Platinum partitioning between metal and silicate melts: Core formation, late veneer and the nanonuggets issue

Etienne Médard, Max W. Schmidt, Markus Wälle, Nicole Keller, Detlef Günther

Platinum partitioning between metal and silicate melts: core formation, late veneer and the nanonuggets issue.

Etienne Médard[1,2*], Max W Schmidt[2], Markus Wälle[2,3], Nicole S Keller[4,5], Detlef Günther[3]

[1] *Laboratoire Magmas et Volcans, Université Blaise Pascal - CNRS - IRD, OPGC, 5 rue Kessler, 63038 Clermont Ferrand, France*

[2]*Institut für Geochemie und Petrologie, ETH Zürich, Clausiusstrasse 25, CH-8092 Zürich, Switzerland*

[3]*Laboratory of Inorganic Chemistry, ETH Zürich, Wolfgang-Pauli-Strasse 10, CH-8093 Zürich, Switzerland*

[4]*University of Iceland, Institute of Earth Sciences, Sturlugata 7, IS-101 Reykjavik, Iceland*

[5]*Research School of Earth Sciences, Australian National University, Canberra, ACT 0200, Australia*

[*]**Corresponding author:**

Etienne Médard
Laboratoire Magmas et Volcans
Université Blaise Pascal – CNRS – IRD, OPGC
5 rue Kessler
F-63038 Clermont-Ferrand Cedex, France
E.Medard@opgc.univ-bpclermont.fr
Phone: +33 686 697 599

Abstract:

High-pressure, high-temperature experiments have been performed at ~1.2 GPa and 1360-2100 °C to investigate the partitioning of Pt between a silicate melt and a metallic melt. Our experiments indicate that nanonuggets encountered in previous experiments are experimental artifacts, formed at high temperature by oversaturation caused by high oxygen fugacity during the initial stages of an experiment. Experiments at high-acceleration using a centrifuging piston-cylinder show that nanonuggets can be removed by gravity during the experiment. Formation of nanonuggets can also be avoided by using initially reduced starting materials. The presence of iron is also a key element in reducing the formation of nanonuggets. Our nanonugget-free data are broadly consistent with previous nanonuggets-filtered data, and suggest that Pt partitioning becomes independent of oxygen fugacity below an oxygen fugacity of at least IW+2. Pt is thus possibly dissolved as a neutral species (or even an anionic species) at low fO_2, instead of the more common Pt^{2+} species present at higher fO_2. Due to low concentration, the nature of this species cannot be determined, but atomic Pt or Pt^- are possible options. Under core-formation conditions, Pt partitioning between metal and silicate is mostly independent of oxygen fugacity, silicate melt composition, and probably also pressure. Partition coefficient during core formation can be expressed by the following equation: $\log D_{Pt}^{M\ metal/silicate} = 1.0348 + 14698/T$ (in weight units). Calculations indicate that the Pt content (and by extension the Highly Siderophile Elements content) of the Earth's mantle cannot be explained by equilibrium partitioning during core formation, requiring further addition of HSE to the mantle. The mass of this late veneer is approximately 0.4 % of the total mass of the Earth (or 0.6 % of the mass of the mantle).

1. Introduction: Highly Siderophile Elements and the nanonugget issue

Highly Siderophile Elements (hereafter referred to as HSE) are a class of transition metals that have a strong affinity for liquid or solid metallic alloys during geochemical processes. The HSE group is usually defined as the group of elements with metal/silicate partition coefficients greater than 10^4 at 1 bar, and includes Au, Re, and the platinum group elements (Ru, Rh, Pd, Os, Ir, Pt). Their geochemical affinity for metals makes the HSE excellent tracers for core formation processes in the terrestrial planets, since they are strongly partitioned into the core forming Fe-alloy. Some of the HSE are also involved in key radioisotope systems ($^{190}Pt/^{186}Os$, $^{187}Re/^{187}Os$, $^{107}Pd/^{107}Ag$, Carlson et al., 2008).

The most simple core formation models for the Earth involve equilibration between core-forming metal and mantle-forming silicate melts in a high-temperature magma ocean (see Ringwood, 1977, and a recent review in Righter, 2011). If core segregation was a simple equilibrium process, then the chemical composition of the mantle would record the last equilibration of the two melts at the base of the magma ocean. Since partition coefficients for various siderophile elements vary strongly as a function of temperature, oxygen fugacity, and for some of them possibly pressure (e.g., Ni and Co, Chabot et al., 2005), it would be possible to extract equilibrium conditions from the actual composition of the Earth's mantle combined with a reasonable assumption on bulk Earth composition. The mantle content of moderately siderophile elements can indeed be reproduced by high-temperature equilibration at lower mantle pressures (e.g., ~30 GPa and ~3300 K, Bouhifd and Jephcoat, 2011; Righter, 2011). A more complex class of core formation models involves heterogeneous accretion during which the oxygen fugacity and/or the composition of accreted material change (Rubie et al., 2011; Wade and Wood, 2005). Incomplete equilibration of the latest accreted material may add further complexity (Rubie et al., 2011). One important cornerstone of these models is the partitioning of the moderately siderophile elements; however, they can generally not account for the highly siderophile element concentrations of the Earth's mantle.

HSE concentrations in the Earth's mantle (~0.005-0.009 times CI-chondrites concentrations, Becker et al., 2006; Palme and O'Neill, 2003) are low, yet higher than predicted by equilibrium core formation processes. Nevertheless, for most HSE, partitioning data are scarce and most metal-silicate partition coefficients are derived from solubility experiments in iron-free systems which may or may not apply to the formation of an iron-rich core. For example, only three Pt partitioning studies using Fe- and Mg- bearing compositions

have been published so far (Bennett et al., 2014; Cottrell and Walker, 2006; Mann et al., 2012).

Secondly, most of the HSE show nearly chondritic element ratios in the mantle despite their diverse geochemical behavior (Becker et al., 2006; Lorand et al., 2008). These observations have led to a long-standing controversy between two schools of thought: (1) HSE concentrations in the mantle are the result of core formation processes, either under conditions not yet investigated experimentally or through complex, possibly non-equilibrium processes; (2) very low HSE concentrations in the mantle acquired through core formation processes are overprinted by the later addition of (oxidized) material that does not contribute to core formation (the "late veneer", Chou, 1978).

However, despite experimental and analytical progress, the partitioning of HSE between silicate melts and metallic melts/alloys is still poorly known under the expected geological high-pressure, high-temperature conditions (Ertel et al., 2008) which include variable oxygen fugacity (from ≤ IW-2 for core formation to ~FMQ for upper mantle melting). In the case of Pt, probably the best studied HSE, the first studies at atmospheric pressure (Amossé and Allibert, 1993; Borisov and Palme, 1997; Ertel et al., 1999; Fortenfant et al., 2003) were limited to 1550 °C by the eutectic melting of the Pt-Fe alloy loops used for the experiments. High-pressure experiments (Ertel et al., 2006; Holzheid et al., 2000) expended the range of investigated conditions, but were limited in temperature by the use of Pt capsules and in oxygen fugacity by the presence of nanonuggets. HSE concentrations in experimental silicate glasses are indeed often characterized by a very poor reproducibility, in particular at low concentrations, i.e., at low oxygen fugacities and temperatures. Time-resolved analyses by LA-ICP-MS produce noisy signals characterized by spikes or broad hills and highly unstable count rates (Ertel et al., 2008; Keller, 2008; O'Neill et al., 1995). Those hills and spikes have been attributed to the presence of small metal particles or "nanonuggets", with estimated sizes between 50 nm and 10 µm (e.g., Cottrell and Walker, 2006; Ertel et al., 1999; Fortenfant et al., 2006; Simon et al., 2007). The origin of these nanonuggets has been a matter of heated debate and they have been variably interpreted as (1) quench phenomena (Cottrell and Walker, 2006; Simon et al., 2007), or (2) equilibrium particles resulting from physical processes during the experiment (Borisov and Palme, 1997; Ertel et al., 2008; Ertel et al., 2006; O'Neill et al., 1995). Whether these nanonuggets are considered to be present at run temperature (and thus excluded from the bulk concentration) or quench phases (and thus re-integrated into the bulk concentration) results in orders of magnitude of variation in partition coefficients for platinum group elements (Cottrell and Walker, 2006; Ertel et al., 2006).

Identifying the nature and the formation processes of nanonuggets is thus a key issue for high-quality HSE partitioning data.

In this paper, we investigate Pt partitioning between natural Fe-bearing silicate melt and metallic melt/alloy as a function of temperature and oxygen fugacity at pressures of 0.7 – 1.8 GPa, and temperatures between 1360 and 2100 °C. The main goals are to understand the nature of nanonuggets and the processes that lead to their formation, and to develop a model for Pt partitioning. As a by-product, we also developed new techniques to produce nanonugget-free HSE-bearing silicate glasses at high pressures and temperatures. The results are then used to estimate the need for a late-veneer during the last stage of Earth accretion.

2. Experimental and analytical techniques

2.1. Starting materials

All experiments have been performed in piston-cylinders using high-purity graphite capsules. Three basaltic starting materials with near-identical major element compositions were used (Table 1): (1) for most experiments, a natural high-alumina tholeiitic basalt (82-72f, Donnelly-Nolan et al., 1991), (2) an oxidized Pt-bearing glass made from the natural basalt, and (3) a synthetic Pt-free reduced glass. The oxidized Pt-rich glass was made by attaching powdered 82-72f basalt onto a Pt-wire loop using polyvinyl alcohol as a binder, and glassing it at 1350 °C in air for 48 hours. Under those conditions, ~70 mol% of the iron is expected to be present as Fe^{3+} (Kress and Carmichael, 1991), and the glass is enriched in Pt (3.2 ± 0.7 ppm Pt measured by LA-ICP-MS, Table 1). The reduced, Pt-free glass was made from a gel, burned at 800 °C in air for 48 hours in an alumina crucible, then reacted with pure metallic Fe in a graphite capsule at 1400 °C and 1.2 GPa for more than 48 hours in a piston-cylinder. At the end of the experiments, this silicate glass is in equilibrium with a Fe-C alloy containing 5.3 ± 0.2 wt% C, at an oxygen fugacity around IW-0.7 (Médard et al., 2008). Special care was taken that no Pt came into contact with this starting material and the Pt concentration in the reduced glass is below the detection limit of LA-ICP-MS (~4 ppb, Table 1).

2.2. Static experiments

Static experiments have been performed in 14.0 mm bore, end-loaded solid-medium piston-cylinder devices at ETH, at a constant pressure of 1.2 GPa and temperatures from 1360 to 2100 °C. A regular talc-Pyrex-graphite-MgO assembly has been used up to 1600 °C. For higher temperature experiments to 2100 °C, Pyrex was replaced by SiO_2-glass. The experimental samples were prepared by putting small clippings of high-purity Pt wire (99.95 %) at the bottom of a graphite container, and packing ~25-30 mg of basalt starting material on top. High-purity Fe metal or powdered Fe_2O_3 was also added together with the Pt in some experiments (Table 2). For experiments at 1360-1400 °C, the graphite container was encased in a Pt capsule that had been triple crimped, welded shut and flattened on one end. Graphite powder was packed above and below the graphite capsule, then the top of the outer Pt capsule was crimped and welded shut. No outer Pt capsule was used at ≥ 1600 °C. Capsules were fitted in an alumina sleeve and positioned in the hotspot of a straight-walled graphite furnace using MgO spacers. Pressure calibration based on the reactions coesite = quartz (Bose and Ganguly, 1995) and fayalite + quartz = ferrosilite (Bohlen et al., 1980) resulted in a 10% friction-correction for the talc-Pyrex assembly. No pressure calibration has been done for the talc-SiO_2 assembly; we assume a correction similar to the talc-Pyrex assembly. Pressures are thought to be accurate within ± 0.01 GPa, the oil pressure acting on the piston being held automatically within ± 0.2 bar during the entire experiment. Temperature was monitored using either type B thermocouples ($Pt_{94}Rh_6$-$Pt_{70}Rh_{30}$) to 1600 °C, or type C thermocouples ($W_{97}Re_3$-$W_{75}Re_{25}$) at ≥1700 °C, with no correction for the effect of pressure on thermocouple emf, and was controlled to within ± 2 °C of the setpoint using an Eurotherm controller. Temperatures are thought to be accurate within ± 10 °C. Experiments were pressurized at room temperature to 0.4 GPa, after which the temperature was raised at 50 °C/min to the target temperature. When temperature reached ~ 700 °C (for the Pyrex-bearing assembly) or ~ 1000 °C (for the SiO_2-glass assembly), pressure was raised to the target pressure and held constant. Experiments were terminated by shutting off heating power to the apparatus. Experimental conditions are presented in Table 2.

Three experiments (B1072, B1087 and B1092) already reported by Médard et al. (2008) were performed in a 12.7 mm bore piston-cylinder at MIT, using $BaCO_3$ assemblies. Another experiment (C1006) and syntheses of the reduced glass were run in a 19.1 mm piston-cylinder at LMV, Clermont-Ferrand, using salt/Pyrex assemblies and following the same experimental procedures than Médard et al. (2004).

187 *2.3. Dynamic experiments*

188

189 Dynamic experiments (Table 3) were run at ETH using a miniaturized 14 mm bore
190 non-endloaded piston-cylinder mounted on a centrifuge (Ardia et al., 2008; Schmidt et al.,
191 2006). This setup allows the experimental sample to be accelerated to 1500 g at a rotation of
192 ~2000 rpm and a sample position at ~327 mm radius. The centrifugation increases the settling
193 velocity of solid particles (for example metallic nuggets) present during the experiment such
194 that Pt-nuggets of 0.1 μm diameter should settle at ~0.5 mm/h at 1500 *g* acceleration.
195 Dynamic experiments are two stage experiments: a first static equilibration experiment is run
196 in a regular endloaded piston-cylinder. The sample is then transferred into a new assembly
197 and run in the centrifuging piston-cylinder at high acceleration. Assemblies, thermocouples,
198 and temperature control are identical for the static and the centrifuging experiments.
199 Pressure can be monitored but not modified during centrifuging. A second limitation is
200 posed by the fact that heating is only advisable when centrifuging (at a minimum of 200 rpm).
201 The experiment is thus first pressurized to 0.4 GPa, heated at low acceleration to the
202 temperature of glass softening (~ 700 °C for Pyrex, ~1000 °C for SiO_2 glass), quenched,
203 pressurized to a target pressure lower than the final pressure to account for thermal expansion,
204 and then simultaneously heated to the final temperature and brought to the final acceleration.
205 This procedure can result in a significant deviation from the nominally desired pressure
206 (Table 3).

207

208 *2.4. Major element analysis*

209

210 All experiments contain a silicate glass and a metallic bead (Fig. 1a). These were
211 analyzed for major elements with the JEOL JXA-8200 electron microprobe at ETH. On-line
212 data reduction was accomplished using the φρZ correction procedure. For silicate glasses, a
213 10 nA beam current, 15 kV accelerating potential and 20 μm beam diameter were used for all
214 analyses. Calibration was performed on natural and synthetic oxides and silicates. Metallic
215 alloys were first analyzed using a 30 nA beam current, 15 kV accelerating potential, and 20
216 μm beam diameter, with pure Pt (Mα line) and Fe (Kα line) metals as standards. Many
217 metallic alloys are liquid under experimental temperature and quench to a fine-grained, multi-
218 phased mix (Fig. 1b). However, using a 20 μm defocused beam results in homogeneous
219 individual analyses each representing average values of the liquid alloy composition.

Experimental alloys with low microprobe totals were re-analyzed with a procedure including carbon on the CAMECA SX-100 electron microprobe at LMV. Graphite-saturated cohenite (Fe_3C) was synthesized at 1.5 GPa and 1200 °C for 46 h in a graphite capsule (Tsuzuki et al., 1984) and used as a carbon standard, together with pure Pt and Fe metals. Walker et al. (2013) have shown that Fe_3C is non-stoichiometric: under conditions similar to our experimental conditions (1 GPa and 1210 °C), graphite-saturated Fe_3C contains 6.9 wt% C (25.7 at% C), compared to the stoichiometric value of 6.7 wt%. Since our alloys are conductive, carbon paint was carefully applied such that just the rim of the alloy was covered. This allows for charge transfer during the analysis (Chabot et al., 2008) but avoids carbon contamination. Carbon concentrations were analyzed on a PC2 spectrometer. Due to the presence of high order Pt L_α and Fe K_α peaks near the C K_α peak, the background correction was taken as the height of the C K_α peak for C-free standards (Fe and Pt), instead of the usual background measurements on both sides of the peak.

2.5. Platinum in glasses

Pt concentrations in silicate glasses were analyzed by LA-ICP-MS, using a Ti:sapphire femtosecond laser system (Legend, Coherent Inc., Santa Clara, CA, USA) on its fundamental wavelength, coupled to an Elan DRC II (PerkinElmer SCIEX, Thornhill, Canada) ICP-MS. The analytical conditions are given in Table 4. ^{178}Hf was measured to ensure that HfO interference on the Pt isotopes can be excluded since the natural starting material contained small amounts of Hf. The laser beam was focused using a plano-convex lens (f = 75 mm) and the focal point was kept slightly (~0.5 mm) below the sample surface. A cylindrical ablation cell with a volume of ~40 cm^3 was used. For standardization, NIST 612 (2.59 ppm Pt) was used as external standard and ^{42}Ca as internal one, using the CaO concentration derived from the microprobe data. The concentrations of NIST 612 were taken from the GeoReM database (http://georem.mpch-mainz.gwdg.de, Jochum et al., 2005). Three major Pt isotopes (^{194}Pt, ^{195}Pt, ^{196}Pt) were analyzed and the three concentrations calculated from each isotope were averaged, since the variation in the three different measurements was lower than the one between different measurements. A minimum of three widely spaced spots were analyzed in each experimental sample.

3. Results

253 *3.1. Experiments using natural starting material*

254

255 Twenty-one experiments were performed on the natural basaltic starting material, with
256 temperature varying from 1360 to 2100 °C and oxygen fugacity from ΔIW = -2.0 to +2.6,
257 where ΔIW[1] is the oxygen fugacity difference between the experiment and the iron-wüstite
258 (IW) buffer (Campbell et al., 2009), expressed in log units. This variation in experimental
259 oxygen fugacity was achieved by adding variable amounts of metallic Fe in addition to Pt
260 (Grove, 1981; Médard et al., 2008). Fe_2O_3 powder was also added in a few experiments to
261 maintain high oxygen fugacities. For a given temperature and pressure, there is a rough
262 correlation between the composition of the added metal and the oxygen fugacity (Fig. 2).
263 Oxygen fugacity can be tuned over 4 orders of magnitude, however, it is limited by two
264 constraints: (1) at high oxygen fugacity, use of a graphite capsule forbids oxygen fugacities
265 higher than that imposed by the graphite / CO / CO_2 equilibrium (i.e. the CCO buffer,
266 Jakobsson and Oskarsson, 1994); and (2) the lowest possible oxygen fugacity that can be
267 reached is when the metallic alloy does not contain any Pt (pure Fe with some dissolved C).
268 All experiments contain a homogeneous silicate glass of basaltic composition and a
269 single bead of metallic alloy (Table 5). Depending on temperature and oxygen fugacity, two
270 types of metallic alloys were analyzed: (1) at low temperature and high fO_2 (> IW+0.1 at
271 1400 - 1600 °C), solid alloy beads are homogeneous, have an oblong shape and do not contain
272 any detectable amount of carbon (below the 0.06 wt% detection limit of the microprobe); (2)
273 at higher temperature (T > 1600 °C) or lower oxygen fugacity, liquid alloy beads are perfectly
274 spherical and quench to a dendritic intergrowth of phases variously enriched in Pt, Fe, and C.
275 Carbon concentrations are always above detection limit. The composition of the crystalline
276 alloy, present between 1360 and 1600 °C varies from X_{Fe} (molar Fe/(Fe+Pt+C)) = 0.30 to
277 0.54. This variation results from the starting material: those experiments with metallic Fe
278 added have higher Fe-concentrations in the Pt-Fe alloy and lower oxygen fugacities. Liquid
279 alloys, present in experiments between 1380 and 2100 °C (Fig. 1b), have an X_{Fe} of 0.71 to
280 0.80 for those experiments were metallic Fe was added, and a X_{Fe} of 0.48-0.59 for those
281 without added Fe or with Fe_2O_3 added. In the experiments at 1380-1400 °C a liquid results
282 when metallic Fe was added causing > 66 wt% Fe in the alloy, contrasting solid alloys that
283 have < 26 wt% Fe. At 1600-1700 ºC the transition between solid and molten alloy is between

[1] The formulation developed by Campbell et al. (2009) gives the oxygen fugacity of the Fe-FeO equilibrium, hereafter referred to as iron-wüstite (IW) buffer in the paper. Under the pressures and temperatures investigated here, wüstite is however non-stoichiometric, and the real equilibrium between iron and wüstite (O'Neill, 1988) is located on average 0.5 log unit higher than the Campbell IW reference used in our paper.

19 and 22 wt% Fe. The metallic melt contains between <0.5 and 4.5 wt% C, decreasing with increasing Pt-content. Analysis of quenched dendritic liquid alloys results in higher uncertainties than for solid alloys, particularly for C, with the analytical dispersion often reaching 0.5 wt% C, despite a 0.06 wt% detection limit. For Pt-rich liquid alloys with less than 50 wt% Fe, C concentrations are lower than 0.5 wt%, with a 2σ relative error around 100% (Table 5). Setting those values to zero (i.e. neglecting the effect of carbon) results in less than 6% relative error on fO_2 and partition coefficients.

Most experimental glasses show flat LA-ICP-MS time-resolved Pt spectra (Figs. 3a, 4b). Spikes, indicatives of the presence of nanonuggets (Ertel et al., 2008), are only observed in a few samples, often at the edges. When present, the few spikes can easily be avoided when processing the LA-ICP-MS signal. Pt concentrations in all experimental glasses are constant throughout most of the experimental charge. This is unlike previous studies on Pt solubility at low fO_2 (Ertel et al., 2006), and will be discussed in the next section.

3.2. Attainment of equilibrium – reversal experiments

The natural starting material contains some amount of Fe^{3+}, and is likely more oxidized than all of the final experimental products. Our experiments with natural starting material are thus all reduction experiments. Since Pt partitioning is strongly fO_2 sensitive (at least at fO_2 > IW+3, Ertel et al., 1999), a progressive decrease in oxygen fugacity during the experiment could result in an overestimation of Pt concentration if equilibrium were not completely reached. Reversal experiments use a reduced starting glass (log fO_2 = -10.6 = IW-0.7) that is oxidized during the experiments. Four reversal experiments were performed at temperatures between 1400 and 1900 °C (Table 2). Experimental run products are identical to the run products using the natural starting material. No evidence for Pt nuggets has been found in these experiments. Pt concentrations in reversal experiments are within the range of Pt concentration in regular experiments with natural starting material, indicating that equilibrium was achieved in all experiments. Partition coefficients (section 5) are almost identical in experiments run under similar conditions using the reduced and the natural starting material: at 1400 °C, they differ by less than 0.2 log units between experiments C1006 and Z164; at 1600 °C, they differ by 0.5 log units between experiments B966 and B786, and at 1900 °C they differ by 0.2 log units between experiments B967 and B816. Also the results of these reversal experiments indicate that equilibrium Pt concentrations were obtained in all of our experiments.

3.3. Nuggets production by Pt oversaturation

All the above experiments did not produce nanonuggets. To test the hypothesis that nanonuggets may form by Pt oversaturation, as suggested by Fortenfant et al. (2006) for Os, and Bennett et al. (2014) for Pt, two experiments at 1360-1400 °C (B1087 static and Z300 dynamic) were performed with an oxidized starting material that was enriched in Pt (Table 1, Table 2). The two experiments yielded silicate glasses in equilibrium with a solid Pt-rich alloy with ~12 wt% Fe. As will be discussed below, the static experiment yielded charges full of nanonuggets, whereas nanonuggets have been partially removed in the dynamic experiment. These two experiments are useful to elucidate the origin of nanonuggets but cannot be used to determine Pt partitioning.

Two main aspects of the data will be discussed in the following. First we will demonstrate that nanonuggets are high-temperature equilibrium metallic particles, whose formation depends on the experimental oxygen fugacity path. We will then investigate the parameters influencing the partitioning of Pt between silicate melt and metallic alloys, and show that temperature is the dominant factor that controls partitioning.

4. Pt in silicate melts: the nanonuggets issue

From our experiments and a review of the literature, it results that the nugget-issue contains two qualitatively different aspects: the formation of μm-sized Fe-rich microspheres and that of true Pt-rich nanonuggets. These aspects are discussed separately below.

4.1. High-temperature iron microspheres

Our higher temperature experiments (from 1800 °C to 2100 °C) contain μm-sized metallic spheres (Fig. 4a). These particles are clearly distinct from the nanonuggets of Ertel et al. (2008), and, in the following, the term “microspheres” will be used to distinguish them from “true” nanonuggets. The size of the microspheres is a rough function of temperature, the largest ones (up to 2 μm) being observed in run B868 at 2100 °C (Fig. 4a). Electron microprobe analyses indicate that the microspheres are made of pure Fe-metal, with Pt

concentrations below the detection limit (< 0.1 wt%). They are thus not equilibrium particles, as the equilibrium metallic alloys contain significant amounts of Pt (e.g., 35.9 wt% Pt in experiment B868, Table 4) and have Fe activities much lower than unity.

In experiment B868, the 2D-microsphere density can be estimated from SEM electron backscatter images at about 250 / mm². The average diameter of the spheres is 1.7 μm, so all the observed spheres have their centers inside a 1.7 μm thick slice of glass centered on the exposed surface. We thus conclude that the 3D-microspheres density is about 250 / 0.0017 = 15.10^4 / mm^3. With an average crater diameter of 150 μm, and an average depth of 100 μm, about 1000 microspheres should have been ablated during the 30 s of a LA-ICP-MS analysis. However, due to very low Pt concentrations in the microspheres, there is no visible change in the time-resolved Pt-concentrations (Fig. 4b), contrasting with the observations made on true low-temperature nanonuggets (Ertel et al., 2008).

These microspheres show strong similarities with the "micronuggets" of Cottrell and Walker (2006). Both experimental sets use relatively oxidized natural starting materials and similar capsule material and experimental conditions. In our experiments, microspheres are distributed in the entire glass area, whereas Cottrell and Walker (2006) describe a band of "micronugget"-free glass near the sides of their graphite capsules. This is, however, not obvious from their pictures (Fig. 2B), where "micronuggets" are also attached to the sides of the graphite capsule. Such an indication of heterogeneous nucleation is clearly visible in our experiments, where microspheres have a tendency to form at the sides of the graphite capsule, or on pieces of graphite dispersed in the experimental glass (Fig 4c).

In summary, microspheres (1) are observed in experiments at very high-temperature (at or above 1800 °C), (2) have a different composition than the equilibrium metal (but their composition may reflect the Fe/Pt ratio of the glass), and (3) their presence has no influence on the Pt concentration in the silicate melt. We thus conclude that these microspheres are formed upon quench, and were not present during the experiment as equilibrium metallic particles. Microspheres may have been formed by a smelting reaction, as suggested by Cottrell and Walker (2006).

4.2. Nanonuggets-free experiments

With the exception of a few occasional spikes in Pt ablation-spectra near the edge of some samples (which could result from artefacts, see below), no evidence for Pt-bearing nanonuggets was found in our experiments performed with natural starting material. Metal-

385 silicate equilibration experiments on Pt (and other HSE) can be separated in two categories:
386 (1) solubility experiments, where the metallic phase is pure Pt, equilibrated with a Fe-free
387 silicate melt, often with bulk silicate compositions corresponding to the Di-An eutectic
388 (Borisov and Palme, 1997; Ertel et al., 1999; Ertel et al., 2006; Fortenfant et al., 2003), and
389 (2) partitioning experiments, where Pt-bearing metallic Fe is equilibrated with an Fe-bearing
390 silicate melt (Bennett et al., 2014; Cottrell and Walker, 2006; Holzheid et al., 2000; Mann et
391 al., 2012). Nanonuggets have been encountered in all solubility studies using Fe-free systems.
392 They disappear at the highest temperatures and oxygen fugacities, and are increasingly more
393 common towards low temperatures and oxygen fugacities. However, our experiments do not
394 contain any nanonuggets, even at low temperatures (down to 1360 °C) and low concentrations
395 (down to ~10 ppb). Our data are identical to the average lowest Fe-free data of Ertel et al.
396 (2006) under similar conditions (P = 1.0-1.5 GPa, fO_2 ~ CCO buffer), nevertheless without a
397 need for nanonugget filtering. This strongly suggests that Fe plays a key role in nanonuggets
398 formation/dissolution. The absence of nuggets in Fe-bearing versus Fe-free systems is in
399 agreement with the results obtained by Laurenz et al. (2010) on Pd.
400
401 Dynamic experiments have been performed in order to ensure that our experiments
402 where truly nanonugget-free. The average diameter of nanonuggets can be estimated to
403 between 50 nm and 1 µm (Ertel et al., 2008; Ertel et al., 1999; Fortenfant et al., 2006).
404 Assuming that Stokes' law can be applied to such small particles, a calculated particle density
405 of 18 $g \cdot cm^{-3}$ ($Pt_{75}Fe_{25}$ alloy) and a basalt density and viscosity of 2.9 $g.cm^{-3}$ and 1 Pa·s (at
406 1400 °C, Giordano et al., 2008) lead to settling rates of the nanonuggets between 0.1 and 30
407 $\mu m.h^{-1}$. By using a centrifuging piston-cylinder, settling rates can be multiplied proportionally
408 to the g-force applied such that complete segregation of nanonuggets from the silicate melt
409 can be reached within a few hours (settling velocities between 150 and 45 000 $\mu m.h^{-1}$ at 1500
410 g). Experiment Z164, centrifuged at 1500 g for 11 hours results in a very homogeneous
411 capsule interior, with possible evidence for nanonuggets only on the rims of the sample.
412 Using only the interior spots, Z164 results within error in the same Pt concentration than the
413 corresponding static experiment (37±5 ppb instead of 33±4 ppb for experiment B1072). The
414 centrifuging should have moved even the smallest nanonuggets by more than a millimeter;
415 hence nanonuggets did not form in experiments with the natural starting material. The
416 presence of Pt spikes near the edges of samples, also observed in static experiments, may
417 result from a preferential nucleation of nanonuggets near the graphite-silicate melt interface or
418 by submiscroscopic Pt impurities caught during polishing between the soft graphite and the

419 silicate glass and are judged to represent artefacts. Overall, no difference was observed
420 between static and dynamic experiments using the natural starting material, strongly
421 indicating that nanonuggets were not present during these experiments.
422
423 *4.3. Formation and resorption of Pt-rich nanonuggets*
424
425 Experiment B1087, using the Pt-rich oxidized starting material, produces an extremely
426 nugget-rich charge, in which an equilibrium Pt concentration in between the nuggets cannot
427 be measured (Fig. 3b). As in experiments with natural starting material, the oxygen fugacity is
428 reduced through reaction between the silicate glass and the graphite capsule until reaching
429 equilibrium near the CCO oxygen buffer. The only differences between the two types of
430 experiments are the higher initial oxygen fugacity in the oxidized starting glass, and the Pt
431 concentration in the starting glass: the oxidized starting glass, Pt-saturated in air, contains 3.2
432 ppm dissolved Pt (Table 1), whereas the natural glass contains a very low amount of Pt
433 (below 4 ppb, Table 1). It is thus likely that nanonuggets formed from the Pt-rich material as a
434 consequence of Pt-oversaturation during reduction, since Pt solubility is strongly dependent
435 on oxygen fugacity at moderate to high fO_2 (at least above CCO, Borisov and Palme, 1997). It
436 should be noted that for all experiments in which nuggets have been encountered, the final
437 experimental fO_2 is systematically lower than the initial fO_2 of the starting material: (1) in
438 CMAS experiments, the starting material is a glass synthesized in air (Amossé and Allibert,
439 1993; Borisov and Palme, 1997; Ertel et al., 1999; Ertel et al., 2006; Fortenfant et al., 2003),
440 and (2) experiments in Fe-bearing systems (e.g., Cottrell and Walker, 2006) used natural
441 starting materials, which likely contain small amounts of Fe^{3+}. Since equilibrium Pt
442 concentrations are very small, any Pt that is present in the glass at the beginning of the
443 experiment, or that dissolves in the glass at the initially high oxygen fugacity will result in Pt-
444 oversaturation in the silicate melt at equilibrium, and hence in subsequent precipitation of
445 equilibrium nanonuggets. Comparison between experiments using the natural, Pt-poor,
446 starting material, and experiments using Pt-enriched starting material confirm that
447 nanonuggets are equilibrium particles formed through oversaturation of the silicate melt upon
448 reduction.
449
450 Once formed, nanonuggets can only be removed by two different mechanisms: physical
451 segregation or Ostwald ripening. Nanonuggets that formed in the experiment using the Pt-
452 bearing oxidized starting glass did not settle by gravity, even after 72 hours. The experiment

was duplicated with an equilibration time of 48 h, then centrifuged for 7h at 1000 g to remove the nanonuggets (experiment Z300, Table 3). According to Stokes' law, a 50 nm diameter nanonugget should have moved by at least 0.5 mm during the experiment. Time-resolved LA-ICP-MS analyses of experiment Z300 are presented in Fig. 5. In the static experiment B1087, Pt concentrations are highly variable, but on average similar to the initial Pt concentration of the starting material, and well above the equilibrium concentration. Concentrations in the dynamic experiment Z300 are on average significantly lower, with no spot above the initial concentration of the starting material (Fig. 5). They are, however, at least one order of magnitude above the expected equilibrium concentration. The minimum concentration measured in experiment Z300 is 150 ppb, compared to 19-37 ppb in equilibrium experiments under similar conditions, and > 1000 ppb in experiment B1087. These results indicate that nanonuggets were partially removed by centrifuging, but less than would be expected for 50 nm diameter particles obeying Stoke's law. It is possible: (1) that nanonuggets in our experiment are smaller than 50 nm. This value was proposed for example by Ertel et al. (1999), but if nanonuggets formed by oversaturation, their size should depend on the initial Pt concentration, the diffusion rate of Pt (i.e. the temperature) and the amount of oversaturation. Smaller nanonuggets could be present in our experiment, which is characterized by extreme oversaturation and low temperature (1400 °C); (2) that Stokes' law does not fully apply to such small particles; (3) that the settling of nanonuggets is hampered by small temperature gradients in the experiment which could induce a convective flow in the sample. Even if smaller than expected, the evidence for physical segregation demonstrate that nanonuggets can be formed by oversaturation and removed by physical processes.

Assuming that nanonuggets are formed during the experiments as a result of a local Pt oversaturation in the melt, the only driving force to remove them is interfacial energy minimization, resulting in Ostwald ripening: growth of the large metal beads at the expense of smaller nanonuggets. After formation, nanonuggets will be eliminated in a 3-step process: (1) detachment of a Pt atom from the metallic nugget and dissolution into the silicate melt, (2) diffusion of Pt in the silicate melt, and (3) attachment of the Pt atom to a larger equilibrium metal phase. When equilibrium Pt solubilities in the silicate melt are very low, diffusion represents the limiting step, as only a very small number of Pt atoms are dissolved and may diffuse at any given time. The lower the equilibrium concentration, the higher the chances of preserving nanonuggets, as observed in all previous experimental studies (e.g., Ertel et al., 2008). Nanonuggets could then in theory form through oversaturation with any transition

element, in experiments where the oxygen fugacity decreases during the experiment. The lower the element concentration in the silicate melt, and the lower the diffusion coefficient, the more difficult it will be to remove nanonuggets during an experiment. This would explain why nanonuggets are mainly encountered with the least soluble elements (the HSE), at their lowest possible concentrations (i.e., low T and low fO_2). If Pt is dissolved in an ionic form (Pt^{2+} or Pt^{-}, see below), step (1) requires an oxidation or a reduction of Pt°. This redox reaction can only proceed in the presence of a redox partner, e.g. other multiple valence elements like Fe. This key role would explain the rarity of nanonuggets in Fe-bearing experiments compared to Fe-free experiments.

5. Pt-partitioning between metal and silicate

5.1. Activity models

Nernst partition coefficients, calculated from measured mass or molar concentrations are only useful at low concentrations where Henry's law is valid. To account for the large range in experimental FePt-alloy compositions, and in order to apply the experimental data on Pt-rich alloys to the low Pt concentrations relevant to core formation processes, we use partition coefficients based on activities:

$$D_{Pt}^{metal/silicate} = \frac{a_{Pt}^{metal}}{a_{Pt}^{silicate}}$$

This approach requires the calculation of activity coefficients for Pt in alloys and in silicate melts. For silicate melts, Pt concentrations are always <1 ppm, and activities are assumed to be proportional to concentrations according to Henry's law (the value of the constant h will be set to 1 in the following):

$$a_{Pt}^{silicate} = h \cdot X_{Pt}^{silicate} \qquad (1)$$

For solid alloys, an activity model in the Pt-Fe system at 1200 – 1400 °C has been proposed by Kessel et al. (2001). Their asymmetric regular solution model was used here, and is in good agreement (maximum deviation 25 %) with the values at 1375 °C given by Franke and Neuschütz (2005). Comparison between solid alloy data from Kessel et al. (2001) and data for the liquid phase (Franke and Neuschütz, 2005) at 1775 °C show similar X-*a* relations for high Pt concentrations (X > 0.5), but slight differences at low concentrations, with relatively higher

activities of Pt (for a given X) in the liquid alloy. Indeed, liquid alloys are expected to be closer to ideality than solid alloys, i.e. activity coefficients are expected to be closer to unity. A model for the liquid Pt-Fe alloy was thus constructed by fitting an asymmetric regular solution model to the activity data of Franke and Neuschütz (2005).

The use of graphite capsules provided a source of carbon that may dissolve in the Pt-Fe alloy. This effect is negligible for solid alloys due to the very low solubility of carbon in Pt (Watson, 1987), and because all investigated solid alloys are Pt-rich. However, liquid alloys can contain large amounts of dissolved carbon (up to 4.5 wt%, Table 5). For the Pt-Fe-C liquids, a ternary asymmetric regular solution model was constructed after Andersen and Lindsley (1981), assuming pressure-independent Margules parameters and no ternary interaction components. Margules parameters were obtained by fitting asymmetric regular solution models to the data of Franke and Neuschütz (2005) for the three individual binaries (Pt-Fe, Pt-C and Fe-C), following the same approach as Mann et al. (2012). Margules parameters include a temperature dependency to account for the large range of investigated temperatures:

$$W_G = W_H - TW_S \qquad (2)$$

$$W_H^{FePt} = -267.6\ kJ.mol^{-1},\ W_H^{PtFe} = -205.6\ kJ.mol^{-1},\ W_H^{PtC} = 228.3\ kJ.mol^{-1},\ W_H^{CPt} = 100.4\ kJ.mol^{-1},$$
$$W_H^{FeC} = 93.2\ kJ.mol^{-1},\ W_H^{CFe} = -23.7\ kJ.mol^{-1}$$

$$W_S^{FePt} = W_S^{PtFe} = -72.0\ J.mol^{-1}.K^{-1},\ W_S^{PtC} = 24.6\ J.mol^{-1}.K^{-1},\ W_S^{CPt} = 51.5\ J.mol^{-1}.K^{-1},$$
$$W_S^{FeC} = W_S^{CFe} = 0$$

5.2. Pt valence in silicate melts

The dissolution of metals in silicate melts is often assumed to occur through formation of a metal oxide. The valence of a dissolved metal can then be estimated from the partitioning as a function of oxygen fugacity as follows (e.g., Borisov et al., 1994):

$$Pt_{(metal)} + n/4\ O_2 = Pt^{n+}O_{n/2(silicate)} \qquad (3)$$

where *n* is the valence of dissolved Pt. The equilibrium constant of this reaction is given by:

$$K = \frac{a_{PtO_{n/2}}^{silicate}}{a_{Pt}^{metal} \cdot f_{O_2}^{n/4}} = \frac{1}{D_{metal/silicate}^{Pt} \cdot f_{O_2}^{n/4}} \qquad (4)$$

By plotting the partition coefficient as a function of oxygen fugacity, all other parameters (temperature, pressure, melt composition) being kept constant, one can solve for the valence of dissolved Pt. Oxygen fugacity in the experiments was derived from Fe partitioning between silicate melt and metal, using the model proposed by Médard et al. (2008). This experimentally calibrated model only accounts for solid Pt-Fe binary alloys. For experiments containing a liquid ternary Fe-Pt-C alloy, an analogous model was used, where the solid alloy activity model was replaced by the asymmetric regular solution model described in part 5.1.

Log/log plots of partition coefficients as a function of oxygen fugacity for three different temperatures (1400 °C, 1600 °C, and 1900 °C) are presented in Fig. 6, together with literature data and their extrapolations at similar temperatures (Bennett et al., 2014; Borisov and Palme, 1997; Ertel et al., 2006; Fortenfant et al., 2003). All three datasets indicate that, for oxygen fugacities below ~10^{-6}, as investigated here, Pt partition coefficients remain constant or decrease with decreasing oxygen fugacity. Hence, Pt would be dissolved in the metallic state as Pt^0 (n = 0) or anionic Pt^- (n=-1). The presence of zero-valence Pt in silicate melts at low oxygen fugacity was initially suggested by early experimental studies on Pt solubility (Amossé and Allibert, 1993), but these data were not reproduced by subsequent studies. Other early studies suggesting the presence of neutral metals in silicate melts (e.g., Colson, 1992; O'Neill et al., 1995) were widely discarded, and the leveling of solubility at low oxygen fugacity was interpreted as a consequence of the presence of nanonuggets (e.g., Ertel et al., 2008). The only evidence for zero-valence metal in silicate melt published so far is for Pd (Borisov et al., 1994), although the samples were analyzed by bulk methods (neutron activation), such that the presence of nanonuggets would go undetected. For Pt, the most recent studies at 1 atm indicate that it dissolves as Pt^{2+} down to at least $fO_2 = 10^{-5}$ at 1400 °C (Borisov and Palme, 1997; Ertel et al., 1999). Experiments at lower oxygen fugacity could not be used for quantification due to the presence of nanonuggets (Fig. 6). Our experiments at ~1400 °C suggest that Pt could be dissolved as Pt^0 for fO_2 lower than $fO_2 = 10^{-7}$ (~ΔIW+3). The transition between Pt^{2+} and Pt^o would occur at slightly higher absolute oxygen fugacities at higher temperatures (Fig. 6). Our data are equally consistent with a negative valence for dissolved Pt (Pt^-), particularly at 1900 °C below $fO_2 = 10^{-6}$ (Fig. 6). A similar trend is shown

583 by the 2000 °C data of Bennett et al. (2014) at even higher fO_2 (Fig. 6). Platinide anions (Pt^-
584 and Pt^{2-}) are stabilized by the strong contraction of the 6s orbital of Pt (Jansen, 2005). They
585 have already been observed in a few ionic compounds (e.g., Karpov et al., 2006), and can thus
586 possibly be stable in silicate melts.
587
588 As discussed above, evidence for nanonuggets is absent in our experiments, except for
589 those starting from the Pt-rich heavily oxidized material, which are not used for the
590 partitioning model. In most experiments, the relatively oxidized (natural) starting material
591 reacts with the added Pt (and Fe) metal and the graphite capsule, resulting in a decrease in
592 absolute oxygen fugacity. Instead, reversal experiments using a reduced starting material are
593 characterized by an increase in absolute oxygen fugacity during the experiment. Pt
594 oversaturation can thus not occur in these experiments. The four reversal experiments give
595 similar results (e.g., Fig. 7) to the equivalent regular experiments, indicating that all of our
596 experiments have indeed reached equilibrium. In previous studies, the loss of correlation
597 between fO_2 and Pt (or other HSE) concentrations at low fO_2 has been taken as an indication
598 of disequilibrium due to the presence of nanonuggets (e.g., Borisov and Palme, 1997; O'Neill
599 et al., 1995). Such a feature can indeed be explained if the lowest fO_2 experiments initially
600 equilibrated at higher fO_2, and the higher Pt concentration failed to re-equilibrate when the
601 oxygen fugacity decreased. The constant Pt solubility below a certain oxygen fugacity would
602 then be an indication of the concentration level below which diffusive re-equilibration
603 becomes too slow to provide equilibrium concentrations within experimental time frames.
604 However, in our experiments, the measured Pt concentrations in the melt do not level out at
605 low oxygen fugacity, but are highly correlated with fO_2, as observed in solubility studies at
606 higher fO_2 (Fig. 7). This strong variation in Pt concentration in the silicate melt is paralleled
607 by a change in composition of the metallic alloy, resulting in a constant or even decreasing
608 partition coefficient.
609
610 The evidence for equilibrium demonstrates that the loss of a correlation between
611 partition coefficient and oxygen fugacity in our experiments cannot be explained by a
612 disequilibrium process, and clearly indicates that at oxygen fugacities relevant for core
613 formation, Pt is indeed dissolved as a neutral species, or even anionic (Pt^-). Progressive
614 decreases in valence with decreasing oxygen fugacity have been observed with many other
615 HSE (e.g., Bennett and Brenan, 2013; Ertel et al., 2008), allthough Pt was so far an exception.
616

617 *5.3. Possible platinum speciation in silicate melts at low oxygen fugacity (< IW+3)*

618

619 The coordination environment of the Pt dissolved in the silicate melt at low fO_2 cannot
620 be constrained from our experiments. Studies arguing for the presence of dissolved metals as
621 neutral atoms (Borisov et al., 1994; Colson, 1992) are controversial. Another option is the
622 presence of Pt complexes: at the extremely low Pt concentrations observed in our
623 experiments, many other trace elements are orders of magnitude more abundant and are
624 available for the formation of coordination complexes. We show below that Pt complexes are
625 unlikely, and that dissolution of Pt atoms or Pt^- anions in the silicate melt is the most likely
626 mechanism to explain the observed constant or decreasing partition coefficient.

627 Since our experiments have been performed in graphite capsules, the presence of neutral
628 or negatively-charged Pt-carbonyl or Pt-carbide complexes (Borisov and Palme, 1996; Ertel et
629 al., 1999) could explain the observed oxygen fugacity behavior. Recent experimental studies
630 of carbon solubility in silicate melts at low oxygen fugacity indeed suggest that metal-
631 carbonyls could become dominant species (Fe-carbonyls, Stanley et al., 2014; Wetzel et al.,
632 2013). However, work by Bennett et al. (2014) showed no correlation between the carbon
633 content of the melt and the Pt concentration at low oxygen fugacity, as would be expected if
634 the dissolution reaction involved carbon.

635 Likewise, sulfur has been shown to have a strong influence on Pd partitioning (Laurenz
636 et al., 2013), and small amount of sulfur could drastically change Pt behavior during core
637 formation. Trace amounts of sulfur are likely present in our natural starting material. Sulfur,
638 however, is an unlikely species in the synthetic starting material. The fact that partition
639 coefficients are identical in experiments run with the natural and the synthetic starting
640 material (e.g., Fig. 7) indicate that sulfur as a ligand will not explain the behavior of Pt in our
641 experiments.

642 Silicon is another potential ligand for Pt complexes. The presence of Au silicides has
643 been proposed by Borisov and Palme (1996). The formation of a Pt silicide is an oxygen-
644 producing reaction (Bennett et al., 2014), and would thus result in an increase in solubility
645 with decreasing oxygen fugacity. However, silicides are only stable at fO2 < IW-5, much
646 lower than our experimental range (e.g., Schmidt et al. 2014).

647

648 *5.4. Temperature dependence*

649

Since all our experiments have been performed at roughly constant pressure (~1.2 GPa) and constant melt composition, and assuming that oxygen fugacity has no effect on partition coefficients below IW+3 (zero valence), our experiments can be used to quantify the effect of temperature on silicate/metal Pt-partitioning. Fortenfant et al. (2003) and Ertel et al. (2006) have shown that Pt solubility increases (and thus Pt partitioning decreases) with temperature. Regression of our entire partitioning dataset (21 data points, Fig. 8a) as a function of inverse temperature gives a correlation coefficient of 0.922. This high correlation coefficient confirms the robustness of our experimental data. If we consider the possibility of an influence of oxygen fugacity (-1 valence), and only use the results within a restricted range of oxygen fugacity (for example, $-6.5 > \log fO_2 > -7.5$, 11 data points, Fig. 8a), the correlation coefficient is improved (0.941) but the correlation does not change significantly. In the following discussion, we thus use the temperature trend based on all the data.

Partition coefficients have a similar slope versus temperature than that calculated from the nanonugget-filtered data of Ertel et al. (2006), and both dataset predict similar results (Fig. 8b). The small difference can be ascribed to the large uncertainty introduced by the necessary nanonugget-filtering in Ertel's low-temperature data. Part of the difference could also be due to a known effect of Fe on HSE partitioning (Laurenz et al., 2010), since the experiments of Ertel et al. (2006) were performed in an iron-free system. Our data are also consistent with the higher pressure Fe-bearing data of Mann et al. (2012) and Bennett et al. (2014). All of these datasets are, however, inconsistent with the experimental dataset of Cottrell and Walker (2006). Their experimental conditions broadly overlapped with ours (oxygen fugacities of IW-1.2 to IW-5.4 at 1940-2500 °C compared to IW-0.4 to IW-2 at 1800-2100 °C in our highest temperature experiments), but the results are different by at least two orders of magnitude (Fig. 8b). The reason for this discrepancy is still unknown, but could possibly be related to the hidden presence of nanonuggets in their experiments.

To test for the possible influence of oxygen fugacity, the entire existing partitioning database has been plotted by oxygen fugacity range in Fig. 8c. No significant trend is visible, although there is a tendency for lower oxygen fugacity experiments to produce lower partition coefficients. This tendency would be in agreement with the possible occurrence of anionic dissolution mechanisms at the lowest oxygen fugacities, as suggested by the 2000 °C data of Bennett et al. (2014) and our 1900 °C data. If this was the case, however, considering that our highest temperature experiments (1800-2100 °C) have an average oxygen fugacity of IW-1.2, and considering that Pt is dissolved as a (-1) species (Fig. 6), a decrease of one order of magnitude in partition coefficient will require a decrease in oxygen fugacity by four orders of

magnitude (see 5.2.), down to IW-5.2. Note that Cottrell and Walker (2006) data all plot at lower partition coefficients, irrespective of their oxygen fugacity.

5.5. Influence of pressure and silicate melt composition

The influence of pressure has not been investigated in our study, since all experiments have been performed in the narrow pressure range of 0.7 to 1.6 GPa. A previous study by Ertel et al. (2006) has shown that pressure has a negligible effect on Pt solubility to at least 16 GPa. Comparison of our data with the datasets of Ertel et al. (2006) at 0.5-16 GPa and Mann et al. (2012) at 3.5 - 18 GPa (Fig. 8b) confirms this finding. An insignificant effect of pressure has also been reported for Pd and Re partitioning (Bennett and Brenan, 2013; Holzheid et al., 2000).

Borisov and Danyushevsky (2011) have shown that changes in silica content have a small influence on Pt solubility. Nevertheless, significant variations were only observed when approaching geologically non-significant silica-free oxide melts. A comparison between our basaltic melts and the peridotitic melts of Mann et al. (2012) does not show any significant difference (Fig. 8b). Moreover, one of our experimental capsules leaked, and the silicate melt was contaminated by the surrounding MgO and Pyrex (experiment Z184): the MgO-content is twice as high as in the starting material and the analytical total of 90 wt% for the resulting silicate glass can be explained by significant quantities of B_2O_3. Despite the different glass composition, partitioning results for this experiment are very similar to those obtained in regular experiments. All these observations suggest that major element composition of the melt has an insignificant influence on Pt partitioning, and that temperature is by far the most important factor.

6. Implications for core formation models

6.1. Pt partitioning at infinite dilution

Early determinations of equilibrium Pt partitioning during core formation were based on extrapolations of atmospheric pressure data at temperatures < 1600 °C (Borisov and Palme, 1997; Ertel et al., 1999; Fortenfant et al., 2003), assuming that Pt dissolves as Pt^{2+} regardless of oxygen fugacity. 1 atm experimental data yielded metal/silicate partition coefficients for

717 oxygen fugacities relevant to core formation around 10^9. With such partition coefficients, the
718 Earth's mantle should have been quantitatively stripped of Pt during core formation. The
719 presence of small but significant amounts of Pt in the mantle (around 0.006 times the
720 chondritic value, Becker et al., 2006) can only be reconciled with equilibrium partitioning if
721 one considers late addition of Pt-bearing material that did not equilibrate with the core (the so-
722 called "late-veneer").

723 Our experiments in combination with available literature data suggest that, at the low
724 oxygen fugacities relevant for core formation processes (fO_2 < IW+2), Pt dissolves as neutral
725 or negatively charged species. Extrapolations based on Pt^{2+} thus strongly overestimate
726 partition coefficients. Our data, as well as those of Ertel et al. (2006), Mann et al. (2012), and
727 Bennett et al. (2014) indicate that temperature is the only significant parameter influencing Pt
728 partitioning in a relatively reduced Earth. Regression of the data in Fig. 8a gives the following
729 temperature dependence of the activity-based partition coefficient D:

730 $$\log D_{Pt}^{metal/silicate} = 0.9396 + 10501/T \quad (5)$$

731 Assuming temperature and pressure-independent Margules coefficients for Pt in liquid Pt-Fe
732 alloys and using the activity data of Franke and Neuschütz (2005), we can derive the activity
733 coefficient for Pt in metallic iron melt at infinite dilution:

734 $$\log \gamma_{Pt}^{\infty metal} = -2844/T \qquad (6)$$

735 Note that this value is for liquid metal, and significantly lower than the one used for solid
736 metal; if extrapolated down to 1300 °C, the activity coefficient is $1.6.10^{-2}$, compared to 3.10^{-5}
737 in solid metal (Gudmundsson and Holloway, 1993). From this, one can derive the
738 concentration-based partition coefficient D^* for Pt at infinite dilution (in mole fraction):

739 $$\log D_{Pt}^{*metal/silicate} = 0.9396 + 13345/T \qquad (7)$$

740 A mass-based partition-coefficient can be obtained by taking into account the molar weight of
741 the metallic core (assumed to be pure iron, M = 55.85 $g.mol^{-1}$) and the average molar weight
742 of mantle-forming oxides (M = 50.71 $g.mol^{-1}$ for Hart and Zindler, 1986, composition). Since
743 both molar weights are similar, the result is almost identical to the mole-based partition
744 coefficient. The commonly used, mass-based Nernst partition coefficient between metal and
745 silicate liquids at infinite dilution is expressed by:

746 $$\log D_{Pt}^{M\ metal/silicate} = 1.0348 + 14698/T \qquad (8)$$

747 When extrapolated to a core-formation temperature of 3300 K (Bouhifd and Jephcoat,
748 2011; Righter, 2011), metal/silicate partition coefficients from Eq. (8) are around 10^5-10^6.
749 Values that explain the abundance of Pt in the mantle by equilibrium core formation models

are around 10^2, three orders of magnitude lower than the experimental values. By varying the equilibrium temperature within reasonable bounds, log D varies from 6.9 at 2500 K to 4.7 at 4000 K, still well above 2. Even if Pt was dissolved as a (-1) species at low oxygen fugacity, a decrease of D by two orders of magnitude would require a decrease of the oxygen fugacity by 8 orders of magnitude. The average oxygen fugacity of our highest temperature experiments (1800-2100 °C), IW-1.2, is, however, similar to the conditions most likely to prevail at the end of Earth's accretion (IW-2, Wade and Wood, 2005). Thus, even if our results are orders of magnitude lower than previous determinations based on 1 atmosphere data, they confirm that equilibrium core/mantle partitioning cannot explain the observed HSE concentrations in the Earth's mantle, hence additional processes that increase the Pt concentration in the mantle are required.

6.2. The mass of the late veneer

Using a simple mass-balance equation, with the mass of the core making up 32.5 % of the total mass of the Earth, a chondrite-normalized Pt concentration in the mantle of 0.006 (mantle composition from Becker et al., 2006; average of all chondrite compositions measured by Horan et al., 2003), and an equilibrium core-segregation temperature of 3300 K (as estimated from the partitioning of moderately siderophile elements, Bouhifd and Jephcoat, 2011; Righter, 2011), an extra 0.60 ± 0.03 wt % of chondritic material needs to be added to the Earth's mantle without sequestration of material to the core to explain the present day mantle composition. This value depends little on the Pt partition coefficient, indicating that any experimental uncertainties or further uncertainties during data reduction (i.e. the exact value of the activity coefficient of Pt in liquid Fe at infinite dilution) will not strongly change the amount of extra material required. The parameter that exerts the strongest control on the amount of late veneer is the ratio of the Pt concentration in the Earth's mantle to that of the added (late veneer) material. By varying this ratio between 0.005 and 0.01 (Becker et al., 2006; Palme and O'Neill, 2003), the amount of late veneer varies between 0.49 and 1.01 wt% of the Earth's mantle. These values are in excellent agreement with values derived from other HSE like Os, Ir and Re (about 0.5 wt% of late veneer, Bennett and Brenan, 2013; Brenan and McDonough, 2009). The calculated value of 0.60 wt% is, however, significantly lower than the amount of volatile-rich chondritic material required to explain the volatile content of the Earth by late veneer addition only (e.g., 2 ± 1 wt%, Marty, 2012). Note that we used a global average of chondrite compositions for our calculations. Selecting a particular set of chondrites

(carbonaceous chondrites, ordinary chondrites, enstatite chondrites) has a negligible influence on the result, except for two classes of carbonaceous chondrites (CI and CM), that contain up to 30% less Pt than the average chondrite (Horan et al., 2003). If the late veneer was of volatile-rich CI chondrites (e.g., Wang and Becker, 2013), our model gives a larger addition of 0.89 wt% of Earth's mantle, somewhat closer to the estimate of Marty (2012). A late veneer of CM chondrites (e.g., Wang and Becker, 2013) would amount to 0.72 wt% of Earth's mantle.

7. Conclusions

This study has evaluated the factors leading to the formation of micro- and nanonuggets in experiments and provides a recipe how to avoid these undesired features. Nanonuggets are present during experiments and result from oversaturation of the silicate melt during initial oxygen fugacity equilibration. True HSE partitioning data can be obtained without encountering the nanonugget problem through avoiding any Pt oversaturation of the silicate liquid in the course of an experiment. The true Pt partition coefficients (and by analogy of any other HSE metal) are generally close to the values derived from the lowest measured Pt concentrations at a given set of T-fO_2 conditions.

Our experimental data confirm that the Pt concentration of the Earth mantle cannot be explained solely by equilibrium metal/silicate partitioning, and requires the late addition of ~0.60 wt% chondritic material to the Earth after core segregation had completed. This late material thoroughly mixed with the mantle, but never equilibrated with the core.

Acknowledgments

P. Ardia and L. Martin helped with the centrifuge experiments, and J.-L. Devidal and J. Langlade with microprobe analyses. This paper benefited from reviews by D. Walker and N. Bennett, and comments by associate editor R. Dasgupta, as well as discussions with U. Mann, A. Bouhifd and J. Van Orman. This project was funded by the Swiss National Science Foundation. This is Labex Clervolc contribution number xxx.

Bibliography

Amossé, J., Allibert, M., 1993. Partitioning of iridium and platinum between metals and silicate melts: evidence for passivation of the metals depending on f_{O2}. Geochimica et Cosmochimica Acta 57, 2395-2398.

Andersen, D.J., Lindsley, D.H., 1981. A valid Margules formulation for an asymmetric ternary solution: revision of the olivine-ilmenite thermometer, with applications. Geochimica et Cosmochimica Acta 45, 847-853.
Ardia, P., Giordano, D., Schmidt, M.W., 2008. A model for the viscosity of rhyolite as a function of H_2O-content and pressure: a calibration based on centrifuge piston cylinder experiments. Geochimica et Cosmochimica Acta 72, 6103-6123.
Becker, H., Horan, M.F., Walker, R.J., Gao, S., Lorand, J.-P., Rudnick, R.L., 2006. Highly siderophile element composition of the Earth's primitive upper mantle: constraints from new data on peridotite massifs and xenoliths. Geochimica et Cosmochimica Acta 70, 4528-4550.
Bennett, N.R., Brenan, J.M., 2013. Controls on the solubility of rhenium in silicate melt: implications for the osmium isotopic composition of Earth's mantle. Earth and Planetary Science Letters 361, 320-332.
Bennett, N.R., Brenan, J.M., Koga, K.T., 2014. The solubility of platinum in silicate melt under reducing conditions: results from experiments without metal inclusions. Geochimica et Cosmochimica Acta 133, 422-442.
Bohlen, S., Boettcher, A., Dollase, W., Essene, E., 1980. The effect of manganese on olivine–quartz–orthopyroxene stability. Earth and Planetary Science Letters 47, 11-20.
Borisov, A., Danyushevsky, L., 2011. The effect of silica on Pd, Pt and Rh solubilities in silicate melts: an experimental study. European Journal of Mineralogy 23, 355-367.
Borisov, A., Palme, H., 1996. Experimental determination of the solubility of Au in silicate melts. Mineralogy and Petrology 56, 297-312.
Borisov, A., Palme, H., 1997. Experimental determination of the solubility of platinum in silicate melts. Geochimica et Cosmochimica Acta 61, 4349-4357.
Borisov, A., Palme, H., Spettel, B., 1994. Solubility of palladium in silicate melts: implications for core formation in the Earth. Geochimica et Cosmochimica Acta 58, 705-716.
Bose, K., Ganguly, J., 1995. Quartz–coesite transition revisited - reversed experimental determination at 500–1200 °C and retrieved thermochemical properties. American Mineralogist 80, 231-238.
Bouhifd, M.A., Jephcoat, A.P., 2011. Convergence of Ni and Co metal–silicate partition coefficients in the deep magma-ocean and coupled silicon–oxygen solubility in iron melts at high pressures. Earth and Planetary Science Letters 307, 341-348.
Brenan, J.M., McDonough, W.F., 2009. Core formation and metal–silicate fractionation of osmium and iridium from gold. Nature Geoscience 2, 798-801.
Campbell, A.J., Danielson, L., Righter, K., Seagle, C.T., Wang, Y., Prakapenka, V.B., 2009. High pressure effects on the iron-iron oxide and nickel-nickel oxide oxygen fugacity buffers. Earth and Planetary Science Letters 286, 556-564.
Carlson, R.W., Shirey, S.B., Schönbächler, M., 2008. Applications of PGE radioisotope systems in geo- and cosmochemistry. Elements 4, 239-245.
Chabot, N.L., Campbell, A.J., McDonough, W.F., Draper, D.S., Agee, C.B., Humayun, M., Watson, H.C., Cottrell, E., Saslow, S.A., 2008. The Fe-C system at 5 GPa and implications for Earth's core. Geochimica et Cosmochimica Acta 72, 4146-4158.
Chabot, N.L., Draper, D.S., Agee, C.B., 2005. Conditions of core formation in the Earth: constraints from nickel and cobalt partitioning. Geochimica et Cosmochimica Acta 69, 2141-2151.
Chou, C.-L., 1978. Fractionation of siderophile elements in the Earth's upper mantle. Proceedings of the 9th Lunar and planetary science conference, 219-230.
Colson, R.O., 1992. Solubility of neutral nickel in silicate melts and implications for the Earth's siderophile element budget. Nature 357, 65-68.
Cottrell, E., Walker, D., 2006. Constraints on core formation from Pt partitioning in mafic silicate liquids at high temperatures. Geochimica et Cosmochimica Acta 70, 1565-1580.
De Bruin, H., Tangtreeratana, M., 1981. Diffusion of palladium into MgO. Journal of Physics and Chemistry of Solids 42, 333-334.
Donnelly-Nolan, J.M., Champion, D.E., Grove, T.L., Baker, M.B., Taggart, J.E., Bruggman, P.E., 1991. The Giant Crater lava-field - Geology and geochemistry of a compositionally zoned, high-alumina basalt to basaltic andesite eruption at Medicine Lake Volcano, California. Journal of Geophysical Research 96, 21843-21863.
Ertel, W., Dingwell, D.B., Sylvester, P.J., 2008. Siderophile elements in silicate melts - a review of the mechanically assisted equilibration technique and the nanonugget issue. Chemical Geology 248, 119-139.
Ertel, W., O'Neill, H.S.-C., Sylvester, P.J., Dingwell, D.B., 1999. Solubilities of Pt and Rh in a haplobasaltic silicate melt at 1300 °C. Geochimica et Cosmochimica Acta 63, 2439-2449.
Ertel, W., Walter, M.J., Drake, M.J., Sylvester, P.J., 2006. Experimental study of platinum solubility in silicate melt to 14 GPa and 2273 K: implications for accretion and core formation in Earth. Geochimica et Cosmochimica Acta 70, 2591-2602.
Fortenfant, S.S., Dingwell, D.B., Ertel, W., Capmas, F., Birck, J.L., Dalpé, C., 2006. Oxygen fugacity dependence of Os solubility in haplobasaltic melt. Geochimica et Cosmochimica Acta 70, 742-756.

876 Fortenfant, S.S., Günther, D., Dingwell, D.B., Rubie, D.C., 2003. Temperature dependence of Pt and Rh
877 solubilities in a haplobasaltic melt. Geochimica et Cosmochimica Acta 67, 123-131.
878 Franke, P., Neuschütz, D., 2005. The Landolt-Börnstein Database (http://www.springermaterials.com).
879 Giordano, D., Russell, J.K., Dingwell, D.B., 2008. Viscosity of magmatic liquids: a model. Earth and Planetary
880 Science Letters 271, 123-134.
881 Grove, T.L., 1981. Use of PtFe alloys to eliminate the iron-loss problem in 1 atmosphere gas mixing
882 experiments: theoretical and practical considerations. Contributions to Mineralogy and Petrology 78, 298-304.
883 Gudmundsson, G., Holloway, J.R., 1993. Activity-composition relationships in the system Fe-Pt at 1300 and
884 1400 °C and at 1 atm and 20 kbar. American Mineralogist 78, 178-186.
885 Hart, S.R., Zindler, A., 1986. In search of a bulk-Earth composition. Chemical Geology 57, 247-267.
886 Holzheid, A., Sylvester, P.J., O'Neill, H.S.-C., Rubie, D.C., Palme, H., 2000. Evidence for a late chondritic
887 veneer in the Earth's mantle from high-pressure partitioning of palladium and platinum. Nature 406, 396-399.
888 Horan, M., Walker, R.J., Morgan, J., Grossman, J., Rubin, A., 2003. Highly siderophile elements in chondrites.
889 Chemical Geology 196, 5-20.
890 Jakobsson, S., Oskarsson, N., 1994. The system C-O in equilibrium with graphite at high pressure and
891 temperature: an experimental study. Geochimica et Cosmochimica Acta 58, 9-17.
892 Jansen, M., 2005. Effects of relativistic motion of electrons on the chemistry of gold and platinum. Solid State
893 Sciences 7, 1464–1474.
894 Jochum, K.P., Nohl, U., Herwig, K., Lammel, E., Stoll, B., Hofmann, A.W., 2005. GeoReM: a new geochemical
895 database for reference materials and isotopic standards. Geostandards Geoanalytical Research 29, 333-338.
896 Karpov, A., Konuma, M., Jansen, M., 2006. An experimental proof for negative oxidation states of platinum:
897 ESCA-measurements on barium platinides. Chemical Communications 2006, 838-840.
898 Keller, N.S., 2008. Metals and volatiles in melts: an experimental and field study. Unpublished PhD thesis,
899 Australian National University, Canberra, Australia.
900 Kessel, R., Beckett, J.R., Stolper, E.M., 2001. Thermodynamic properties of the Pt-Fe system. American
901 Mineralogist 86, 1003-1014.
902 Kress, V.C., Carmichael, I.S.E., 1991. The compressibility of silicate liquids containing Fe_2O_3 and the effect of
903 composition, temperature, oxygen fugacity and pressure on their redox states. Contributions to Mineralogy and
904 Petrology 108, 82-92.
905 Laurenz, V., Fonseca, R.O.C., Ballhaus, C., Jochum, K.P., Heuser, A., Sylvester, P.J., 2013. The solubility of Pd
906 and Ru in picritic melts: 2. The effect of sulfur. Geochimica et Cosmochimica Acta 108, 172-183.
907 Laurenz, V., Fonseca, R.O.C., Ballhaus, C., Sylvester, P.J., 2010. Solubility of palladium in picritic melts: 1. The
908 effect of iron. Geochimica et Cosmochimica Acta 74, 2989-2998.
909 Lorand, J.-P., Luguet, A., Alard, O., 2008. Platinum-group elements: a new set of key tracers for the Earth's
910 interior. Elements 4, 247-252.
911 Mann, U., Frost, D.J., Rubie, D.C., Becker, H., Audétat, A., 2012. Partitioning of Ru, Rh, Pd, Re, Ir and Pt
912 between liquid metal and silicate at high pressures and high temperatures - implications for the origin of highly
913 siderophile element concentrations in the Earth's mantle. Geochimica et Cosmochimica Acta 84, 593-613.
914 Marty, B., 2012. The origins and concentrations of water, carbon, nitrogen and noble gases on Earth. Earth and
915 Planetary Science Letters 313-314, 56-66.
916 Médard, E., McCammon, C.A., Barr, J.A., Grove, T.L., 2008. Oxygen fugacity, temperature reproducibility, and
917 H_2O content for nominally dry piston-cylinder experiments using graphite capsules. American Mineralogist 93,
918 1838-1844.
919 Médard, E., Schmidt, M.W., Schiano, P., 2004. Liquidus surfaces of ultracalcic primitive melts: formation
920 conditions and sources. Contributions to Mineralogy and Petrology 148, 201-215.
921 O'Neill, H.S.-C., Dingwell, D.B., Borisov, A., Spettel, B., Palme, H., 1995. Experimental petrochemistry of
922 some highly siderophile elements at high temperatures, and some implications for core formation and the
923 mantle's early history. Chemical Geology 120, 255-273.
924 O'Neill, H.S.C., 1988. Systems Fe-O and Cu-O: Thermodynamic data for the equilibria Fe-"FeO", Fe-Fe_3O_4,
925 "FeO"-Fe_3O_4, Fe_3O_4-Fe_2O_3, Cu-Cu_2O and Cu_2O-CuO from emf measurements. American Mineralogist 73, 470-
926 486.
927 Palme, H., O'Neill, H.S.C., 2003. Cosmochemical estimates of mantle composition, in: Carlson, R.W. (Ed.),
928 Treatise on Geochemistry. Elsevier-Pergamon, Oxford, pp. 1-38.
929 Righter, K., 2011. Prediction of metal-silicate partition coefficients for siderophile elements: an update and
930 assessment of PT conditions for metal-silicate equilibrium during accretion of the Earth. Earth and Planetary
931 Science Letters 304, 158-167.
932 Ringwood, A.E., 1977. Composition of core and implications for origin of Earth. Geochemical Journal 11, 111-
933 135.

Rubie, D.C., Forst, D.J., Mann, U., Asahara, Y., Nimmo, F., Tsuno, K., Kegler, P., Holzheid, A., Palme, H., 2011. Heterogeneous accretion, composition and core-mantle differentiation of the Earth. Earth and Planetary Science Letters 301, 31-42.
Schmidt, M.W., Connolly, J.A.D., Günther, D., Bogaerts, M., 2006. Element partitioning: The role of melt structure and composition. Science 312, 1646-1650.
Schmidt, M.W., Gao, C., Golubkova, A., Rohrbach, A., Connolly, J.A.D., 2014. Natural moissanite (SiC) – a low temperature mineral formed from highly fractionated ultra-reducing COH-fluids. Progress in Earth and Planetary Science 1:27.
Simon, A.C., Pettke, T., Candela, P.A., Piccoli, P.M., Heinrich, C.A., 2007. The partitioning behavior of As and Au in S-free and S-bearing magmatic assemblages. Geochimica et Cosmochimica Acta 71, 1764-1782.
Stanley, B.D., Hirschmann, M.M., Withers, A.C., 2014. Solubility of C-O-H volatiles in graphite-saturated martian basalts. Geochimica et Cosmochimica Acta 129, 54-76.
Tsuzuki, A., Sago, S., Hirano, S.-I., Naka, S., 1984. High temperature and pressure preparation and properties of iron carbides Fe_7C_3 and Fe_3C. Journal of materials science 19, 2513-2518.
Wade, J., Wood, B.J., 2005. Core formation and the oxidation state of the Earth. Earth and Planetary Science Letters 236, 78-95.
Walker, D., Dasgupta, R., Li, J., Buono, A., 2013. Nonstoichiometry and growth of some Fe carbides. Contributions to Mineralogy and Petrology 166, 935-957.
Wang, Z., Becker, H., 2013. Ratios of S, Se and Te in the silicate Earth require a volatile-rich late veneer. Nature 499, 328–331.
Watson, E.B., 1987. Diffusion and solubility of Pt in C. American Mineralogist 72, 487-490.
Wetzel, D.T., Rutherford, M.J., Jacobsen, S.D., Hauri, E.H., Saal, A.E., 2013. Degassing of reduced carbon from planetary basalts. Proceedings of the National Academy of Sciences of the United States of America 110, 8010-8013.

Figure captions

Figure 1. (a) SEM backscattered electron images of typical run products, with a small bead of quenched liquid Pt-Fe-C alloy surrounded by silicate glass (B815 – 1.2 GPa – 1900 °C); (b) detailed view of quench textures in metallic alloy, showing dendritic growth associated with local variations in Pt (brightest), Fe and C (darkest) concentrations (B816 – 1.2 GPa – 1900 °C). Graphite blades (black) are interpreted as equilibrium graphite crystals and not considered during microprobe analysis of quenched alloys.

Figure 2. Variation of experimental oxygen fugacity as a function of the initially added Fe-Pt metal (X_{Fe} = Fe / (Fe + Pt) in weight). Experiments at ~1400 °C and ~1.2 GPa. The Fe-FeO (IW) reference buffer is from (Campbell et al., 2009), the CCO reference buffer from (Jakobsson and Oskarsson, 1994). The "real" iron-wüstite equilibrium using non-stoichiometric wüstite is also given for comparison (O'Neill, 1988), see note 1).

Figure 3. Time-resolved LA-ICP-MS analysis for two samples run at 1.5 GPa and 1360 °C with different starting materials: (a) experiment B1072 using the natural starting material is nanonugget-free, whereas (b) experiment B1087 run with oxidized and Pt-bearing starting material shows much higher concentration and broad "hills" indicative of nanonuggets.

Figure 4. (a) SEM backscattered electron image showing Fe-microspheres distribution in experiment B868 (1.2 GPa – 2100 °C); (b) time-resolved LA-ICP-MS analysis of sample B868, showing the absence of heterogeneity on the Pt signal; (c) SEM backscattered electron image showing heterogeneous nucleation of Fe-microspheres on the capsule wall.

Figure 5. Time-resolved LA-ICP-MS analyses for samples run at 1.2-1.5 GPa and 1360-1400 °C with oxidized and Pt-bearing starting material. All experiments have been analyzed under the same analytical conditions (25 Hz, 150-200 μm spot size), and the Pt counts is the sum of the counts on the three analyzed isotopes (^{194}Pt, ^{195}Pt, ^{196}Pt). The average number of counts for equilibrium experiments under similar conditions, using either natural (B1072 – 33 ppb Pt) or reduced (C1006 – 19 ppb Pt) starting material is given for comparison. The starting material for the oxidized starting material contains 3.2 ppm Pt. Concentrations in the static experiment (B1087) are highly heterogeneous and on average similar to concentrations in the starting material. Concentration in the central part of the dynamic experiment (Z300) are systematically lower than in the starting material and in the static experiment, but still significantly higher than the equilibrium values.

Figure 6. Metal / silicate partition coefficients (activity-based) as a function of absolute oxygen fugacity for three different experimental temperatures: 1360-1400 °C, 1600 °C and 1900 °C. For two points at 1375-1380 °C and one point at 1600 °C where Pt concentrations in glasses were below detection limit, we used the detection limit and added large error bars to indicate the range of possible values. The slope of the trends strongly suggests that Pt dissolves either as a neutral species or as a Pt^{-} anion under the experimentally investigated conditions, whereas it dissolves as Pt^{2+} under more oxidized conditions. Note that error bars for the activity coefficients are only estimated based on the analytical measurements. True errors including the uncertainties on the calculated activity coefficients are likely larger, but difficult to estimate. For experiments that did not use pure Pt (Bennett et al., 2014; Fortenfant et al., 2003), we used activity coefficients and oxygen fugacities as reported by the authors. For the experiments of Ertel et al. (2006), the oxygen fugacity was assumed to be on the CCO buffer (Jakobsson and Oskarsson, 1994). IW reference from Campbell et al. (2009).

Figure 7. Measured Pt concentrations in silicate melts at 1.2 GPa and 1900 °C as a function of oxygen fugacity. The excellent correlation between concentration and oxygen fugacity (R^2 =

0.957) is a strong indication of equilibrium achievement. Note also that the Pt concentration for the experiments with natural oxidized starting material and the reversal experiments with the reduced synthetic starting material plot on the same line.

Figure 8. Temperature dependence of Pt partition coefficients (activity-based) between metallic and silicate melts. For experiments that used pure Pt or Pt-Fe-C alloys, activity-coefficients were calculated using our ternary model. For other experiments (Bennett et al., 2014; Fortenfant et al., 2003; Mann et al., 2012), we used the activity reported by the authors. (a) Regression of our experimental data. The continuous line is a regression of all 21 data points, the dashed line a regression of the highest oxygen fugacity experiments, which fall into a restricted range of fO_2 ($-6.5 > \log fO_2 > -7.5$). (b) Comparison with previous data show that our experiments are consistent with the 0.5 -14 GPa nanonuggets filtered data of Ertel et al. (2006), the 2.0 GPa data of Bennett et al. (2014), and the 3.5-18 GPa data of Mann et al. (2012), but not with the 2.2-2.3 GPa microprobe data of Cottrell and Walker (2006). For the data of Ertel et al. (2006), only the highest duration experiments were kept at a given pressure and temperature to avoid artifacts linked to incomplete equilibration. The continuous line is the regression of our data from 8a, the dashed line a regression through Ertel et al. (2006) data. (c) The data of 8b have been sorted according to oxygen fugacity relative to the IW buffer. No clear oxygen fugacity trend is visible, but there is a tendency toward lower D at lower oxygen fugacity. All the experiments at $\log fO_2 <$ IW-2.0 come from the same dataset (Cottrell and Walker, 2006).

Tables

Table 1. Starting materials

Sample	natural[a]	oxidized[b]	reduced[b]
SiO_2	47.73	48.2(6)	45.2(5)
TiO_2	0.59	0.61(7)	0.53(13)
Al_2O_3	18.51	18.3(3)	16.9 (3)
FeO*	8.21	8.1(3)	13.7(2)
MgO	10.51	10.50(11)	10.2(4)
CaO	12.01	11.8(2)	11.7(4)
Na_2O	2.16	2.08(16)	2.0(3)
sum	99.72	98.70	99.12
Pt (ppb)	< 4	3200(700)	< 4

[a]Major element analysis from Donnelly-Nolan et al. (1991)

[b]Compositions are microprobe analyses of glasses, renormalized to 100 %; the analytical total is given for information. Values in parentheses are either analytical errors or data dispersions, whichever is the largest, expressed as 2σ. The Pt concentrations have been obtained by LA-ICP-MS (see table 4 for analytical conditions).

Table 2. Static experiments

	starting material (mg)							fO_2
Run#	silicate	Pt	Fe	Fe_2O_3	P (GPa)	T (°C)	[b]hours	(IW)[a]
natural starting material								
B1092	9.9	1.3	0.7		1.5	1360	48.2	0.6
B1072	9.9	0.7			1.5	1360	48.9	2.6
B665	20.2	0.8	10.3		1.0	1380	48.0	-0.9
B772	27.7	0.3	2.5		1.2	1600	20.7	-1.3
B771	29.0	0.7			1.2	1600	43.3	-0.9
B786	26.6	2.1		2.4	1.2	1600	25.8	1.0
B813	28.6	0.2	0.5		1.2	1700	10.1	-1.6
B775	28.2	0.2			1.2	1700	19.0	-0.5
B814	28.1	0.2			1.2	1800	3.2	-1.2
B864	25.2	0.4	9.2		1.2	1900	2.0	-1.9
B862	27.7	2.0	1.9		1.2	1900	2.0	-1.8
B816	26.2	1.8		2.3	1.2	1900	1.5	-1.3
B815	28.6	0.5			1.2	1900	1.5	-0.9
B863	26.7	1.2			1.2	2000	1.5	-1.6
B868	28.8	0.8	1.3		1.2	2100	0.5	-2.1
oxidized starting material								
B1087	9.9	0.8			1.5	1360	72.4	2.6
reduced starting material								
C1006	21.0	6.0			1.2	1400	48.1	2.4
B966	22.5	2.9	0.7		1.2	1600	24.1	-0.1
B967	23.5	1.4	1.0		1.2	1900	2.5	-1.8
B968	25.0	4.6			1.2	1900	2.0	-0.4

[a]Oxygen fugacity is given in log units relative to the IW buffer (Campbell et al., 2009).

[b]Run duration in hours.

Table 3. Dynamic experiments

	starting material (mg)			static step			dynamic step					fO_2
Run#	silicate	Pt	Fe	P (GPa)	T (°C)	hours	P (GPa)	T (°C)	hours	[c]rpm	[c]g unit	(IW)[b]
natural starting material												
Z166	20.9	1.0	12.9	1.0	1400	70.5	0.7	1375	10.4	2017	1488	-0.7
Z164	30.0	3.0		1.5	1400	62.6	1.6	1380	11.1	2020	1492	2.4
Z186	27.1	2.2	[a]2.6	0.5	1600	25.4	0.7	1555	1.3	2014	1480	-0.1
Z184	29.1	1.2		1.2	1600	24.1	1.8	1560	2.1	2015	1481	1.1
Z205	27.5	4.6		1.2	1600	24.8	1.6	1615	1.0	2000	1459	0.9
Z204	25.5	0.7		1.2	1400	49.0	1.1	1655	2.0	2015	1481	1.0
oxidized starting material												
Z300	16.2	0.6		1.2	1400	68.8	1.0	1400	7.0	1300	1000	2.1

[a]In experiment Z186, iron has been added as Fe_2O_3
[b]Oxygen fugacity is given in log units relative to the IW buffer (Campbell et al., 2009).
[c]Acceleration in turns per minute (rpm) and as a multiple of g (9.81 $m.s^{-2}$).

Table 4. Laser and ICP-MS conditions

Laser parameter:

Repetition rate:	25 Hz / 10 Hz; for low or "high" concentration		
Wavelength:	800 nm	Pulse duration:	< 150 fs
Laser energy:	2 mJ	Crater diameter:	120 - 200 µm
Fluency:	6.4 - 17 J/cm^2		

ICP-MS (Perkin Elmer, Elan DRC II):

Nebulizer gas flow:	0.85 L/min Ar	Auxiliary gas flow:	0.85 L/min Ar
Plasma gas flow:	17 L/min Ar	Plasma power:	1400 W
Carrier gas flow:	1 L/min He	Auto lens on	
Isotopes:	^{29}Si, ^{42}Ca, ^{178}Hf, ^{194}Pt, ^{195}Pt and ^{196}Pt		
Dwell time:	10ms (Si, Ca, Hf), 50ms (Pt isotopes)		

Table 5. Experimental results (1360-1560 °C)

Sample	B1087	B1072	B1092	Z166	Z164	B665	C1006	Z300	Z186
starting	oxidized	natural	natural	natural	natural	natural	reduced	oxidized	natural
T (°C)	1360	1360	1360	1375	1380	1380	1400	1400	1555

silicate (wt%)									
SiO_2	48.4(4)	48.7(4)	46.9(8)	46.0(2)	49.9(2)	47.3(2)	45.9(7)	49.7(3)	46.0(3)
TiO_2	0.65(6)	0.62(6)	0.55(8)	0.59(4)	0.62(2)	0.59(4)	0.53(6)	0.63(11)	0.57(2)
Al_2O_3	18.9(2)	19.2(2)	18.2(2)	17.8(2)	19.0(2)	18.2(2)	18.0(3)	18.7(2)	18.1(3)
FeO*	7.0(2)	7.1(2)	11.9(4)	11.6(2)	4.62(9)	9.4(2)	9.1(2)	5.6(2)	11.79(8)
MgO	10.7(2)	10.2(2)	8.9(2)	10.20(9)	11.0(2)	10.4(2)	12.3(3)	10.8(2)	10.2(2)
CaO	11.7(4)	11.5(2)	10.9(4)	11.4(2)	12.3(2)	11.6(2)	12.0(2)	12.2(3)	11.3(2)
Na_2O	2.3(3)	2.42(13)	2.5(2)	2.22(5)	2.23(10)	2.24(11)	2.19(12)	2.1(2)	1.79(16)
sum	98.48	98.40	98.93	98.64	97.57	98.76	96.72	98.96	97.79
Pt (ppb)	nuggets	33(5)	6(2)	≤ 2	37(4)	≤ 2	19(3)	nuggets	39(9)
aFeO	0.0528	0.0539	0.0914	0.0893	0.0348	0.0720	0.0686	0.0426	0.0908
aPtO (10^{-7})		0.0923	0.0179	≤ 0.006	0.1028	≤ 0.006	0.0530		0.1106
alloy (wt%)	solid	solid	solid	liquid	solid	liquid	solid	solid	liquid
Fe	11.8(2)	11.8(2)	25.4(2)	69(2)	11.1(3)	88.2(16)	12.56(12)	12.2(2)	23.1(4)
Pt	88.2(4)	88.2(4)	74.6(4)	29(2)	88.9(5)	7.4(21)	87.4(4)	87.8(8)	76.9(12)
C	≤ 0.06	≤ 0.06	≤ 0.06	2.5(3)	≤ 0.06	4.4(4)	≤ 0.06	≤ 0.06	≤ 0.5
sum	100.7	101.8	102.4	102.4	98.6	101.3	99.8	99.8	98.4
X Fe	0.319	0.319	0.543	0.776	0.304	0.796	0.334	0.326	0.513
X Pt	0.681	0.681	0.457	0.093	0.696	0.019	0.666	0.674	0.487
X C	0	0	0	0.131	0	0.184	0	0	0
aFe	0.008	0.008	0.143	0.547	0.006	0.594	0.011	0.024	0.165
aPt	0.212	0.213	0.025	0.002	0.244	0.001	0.194	0.228	0.048
log fO_2	-7.62	-7.59	-9.63	-11.03	-7.57	-10.91	-7.46	-7.76	-8.56
delta CCO[d]	-0.16	-0.14	-2.18	-2.87	-0.34	-3.60	0.02	-0.28	-1.61
delta IW[d]	2.58	2.61	0.57	-0.72	2.40	-0.91	2.44	2.14	0.10
log D Pt		7.36	7.15	≥ 6.44	7.37	≥ 5.98	7.56		6.63

1084

1085

1086 *Table 5. Experimental results (continued, 1560-1700 °C)*

Sample	[c]Z184	B786	B966	B771	B772	Z205	Z204	B775	B813
starting	natural	natural	reduced	natural	natural	natural	natural	natural	natural
T (°C)	1560	1600	1600	1600	1600	1615	1655	1700	1700
Silicate (wt%)									
SiO_2	41.5(8)	45.2(4)	46.5(4)	48.6(5)	47.7(3)	49.3(4)	49.7(3)	48.5(4)	48.3(4)
TiO_2	0.16(14)	0.53(4)	0.56(14)	0.60(4)	0.58(4)	0.57(4)	0.60(6)	0.59(4)	0.59(4)
Al_2O_3	17(2)	17.8(2)	17.5(3)	18.6(3)	18.40(14)	19.7(2)	18.9(3)	18.83(16)	18.68(14)
FeO*	2.0(6)	11.4(2)	10.7(3)	6.9(3)	8.6(2)	4.59(10)	5.06(14)	7.35(14)	7.07(14)
MgO	24(2)	12.2(2)	10.4(2)	10.9(2)	10.55(12)	10.9(2)	11.0(2)	10.8(3)	10.8(2)
CaO	3.2(9	11.0(3)	12.0(5)	12.1(3)	11.9(4)	12.5(3)	12.3(2)	12.0(3)	12.1(3)
Na_2O	1.77(12)	1.81(8)	2.1(2)	2.19(14)	2.10(8)	2.24(12)	2.26(18)	1.70(10)	2.18(12)
sum	90.00	98.07	99.04	96.98	98.45	99.51	98.36	98.02	98.23
Pt (ppb)	173(6)	84(8)	113(15)	29(4)	≤ 6	182(20)	442(10)	191(6)	< 9
aFeO	0.0162	0.0867	0.0821	0.0525	0.0652	0.0346	0.0382	0.0560	0.0537
aPtO (10^{-7})	0.5015	0.2361	0.3189	0.0810	≤ 0.017	0.5054	1.2294	0.5362	≤ 0.025
alloy (wt%)	solid	solid	solid	liquid	liquid	solid	solid	liquid	liquid
Fe	11.4(4)	18.4(2)	23.8(2)	28.0(4)	85.7(16)	14.1(2)	13.5(2)	22.0(4)	73.5(9)
Pt	88.6(5)	81.6(8)	76.2(6)	72.0(7)	10 (2)	85.9(4)	86.5(4)	78.0(7)	23.4(11)
C[b]	≤ 0.06	≤ 0.06	≤ 0.06	≤ 0.5	4.3(6)	≤ 0.06	≤ 0.06	≤ 0.5	3.1(3)
sum	100.8	100.4	99.8	99.2	100.8	101.1	101.4	97.1	101.9
X Fe	0.310	0.427	0.521	0.576	0.790	0.364	0.355	0.496	0.778
X Pt	0.690	0.573	0.479	0.424	0.026	0.636	0.645	0.504	0.071
X C	0	0	0	0	0.184	0	0	0	0.151
aFe	0.010	0.103	0.141	0.283	0.604	0.025	0.024	0.184	0.599
aPt	0.258	0.126	0.045	0.031	0.002	0.178	0.195	0.076	0.007
log fO_2	-7.19	-7.13	-8.01	-9.00	-9.47	-7.02	-6.79	-7.93	-8.99
delta CCO[d]	-1.29	-0.91	-1.79	-2.78	-3.25	-1.23	-0.80	-2.25	-3.31
delta IW[d]	1.09	1.02	0.14	-0.86	-1.33	0.90	0.96	-0.53	-1.59
log D Pt	6.71	6.65	6.15	6.58	≥ 6.12	6.55	6.20	6.15	≥ 6.43

1087

1088

Table 5. Experimental results (continued, 1800-2100 °C)

Sample	B814	B968	B815	B816	B967	B862	B864	B863	B868
Starting	natural	reduced	natural	natural	reduced	natural	natural	natural	natural
T (°C)	1800	1900	1900	1900	1900	1900	1900	2000	2100
silicate (wt%)									
SiO_2	48.0(3)	48.1(8)	47.7(3)	46.6(2)	45.6(4)	47.6(6)	48.6(4)	47.1(4)	43(2)
TiO_2	0.58(4)	0.57(14)	0.57(4)	0.57(3)	0.48(9)	0.55(4)	0.60(6)	0.58(4)	0.51(4)
Al_2O_3	18.7(3)	18.8(5)	19.3(2)	18.5(2)	19.0(4)	19.3(6)	18.5(3)	20.2(5)	26(2)
FeO*	7.6(2)	7.0(2)	7.47(10)	8.76(14)	10.6(3)	7.68(14)	6.98(14)	7.09(14)	7.2(2)
MgO	10.7(2)	10.9(2)	10.64(16)	11.29(14)	10.3(2)	10.6(2)	10.7(2)	10.7(2)	10.0(2)
CaO	12.0(3)	12.5(3)	11.9(3)	11.8(3)	11.8(3)	11.9(3)	12.1(3)	11.9(3)	11.0(4)
Na_2O	2.21(6)	2.14(14)	2.15(4)	2.19(12)	2.16(13)	2.15(12)	2.17(16)	2.11(14)	1.78(16)
sum[a]	98.89	99.38	98.40	98.37	99.41	99.63	99.94	99.16	99.16
Pt (ppb)	95(6)	735(37)	640(160)	342(30)	210(33)	195(21)	18(2)	504(18)	772(19)
aFeO	0.0576	0.0527	0.0567	0.0665	0.0814	0.0583	0.0530	0.0537	0.0543
aPtO (10^{-7})	0.2826	2.0529	1.7898	0.9566	0.5911	0.5457	0.0503	1.4068	2.1533
alloy (wt%)	liquid	liquid	liquid	liquid	liquid	liquid	liquid	liquid	liquid
Fe	28.7(3)	16.0(4)	20.7(5)	29.2(5)	48.4(9)	55(2)	91.3(7)	27.9(5)	63.1(15)
Pt	71.3(7)	84.0(8)	79.2(8)	70.8(7)	50.4(9)	43(2)	4.2(6)	70.3(8)	36(2)
C[b]	≤ 0.5	≤ 0.5	≤ 0.5	≤ 0.5	[1.2]	1.2(7)	4.5(5)	≤ 0.5	0.84(8)
sum[a]	98.8	99.8	99.3	99.7		101.1	101.6	98.6	100.9
X_{Fe}	0.584	0.400	0.477	0.590	0.710	0.754	0.804	0.581	0.816
X_{Pt}	0.416	0.600	0.523	0.410	0.212	0.169	0.011	0.419	0.133
X_C	0	0	0	0	0.078	0.077	0.185	0	0.051
a_{Fe}	0.368	0.117	0.218	0.414	0.566	0.634	0.658	0.432	0.770
a_{Pt}	0.049	0.201	0.124	0.060	0.028	0.021	0.003	0.078	0.026
log fO_2	-7.93	-6.49	-6.97	-7.39	-7.49	-7.87	-7.99	-7.14	-7.19
delta CCO[d]	-2.73	-1.73	-2.21	-2.63	-2.72	-3.11	-3.23	-2.77	-3.19
delta IW[d]	-1.21	-0.38	-0.85	-1.27	-1.37	-1.76	-1.87	-1.58	-2.14
log D Pt	6.27	5.99	5.84	5.80	5.67	5.58	5.77	5.74	5.09

[a]Silicate melt and alloy compositions are renormalized to 100 %; the analytical total is given for information. Values in parentheses are either analytical errors or data dispersions, whichever is the largest, expressed as 2σ.

[b]The C concentration of solid alloys is below the detection limit of the microprobe (0.06 wt%). For Pt-rich liquid alloys, C cannot be analyzed accurately due to its low concentration (< 0.5 wt%). Values between brackets are estimated from the sums of analyses not including C.

[c]Experiment Z184 is contaminated through interactions with the piston-cylinder assembly. The low total likely indicates presence of boron, originating from the surrounding Pyrex glass.

[d]Oxygen fugacity is given in log units, as absolute value, and relative to the CCO (Jakobsson and Oskarsson, 1994) and IW (Campbell et al., 2009) buffers.

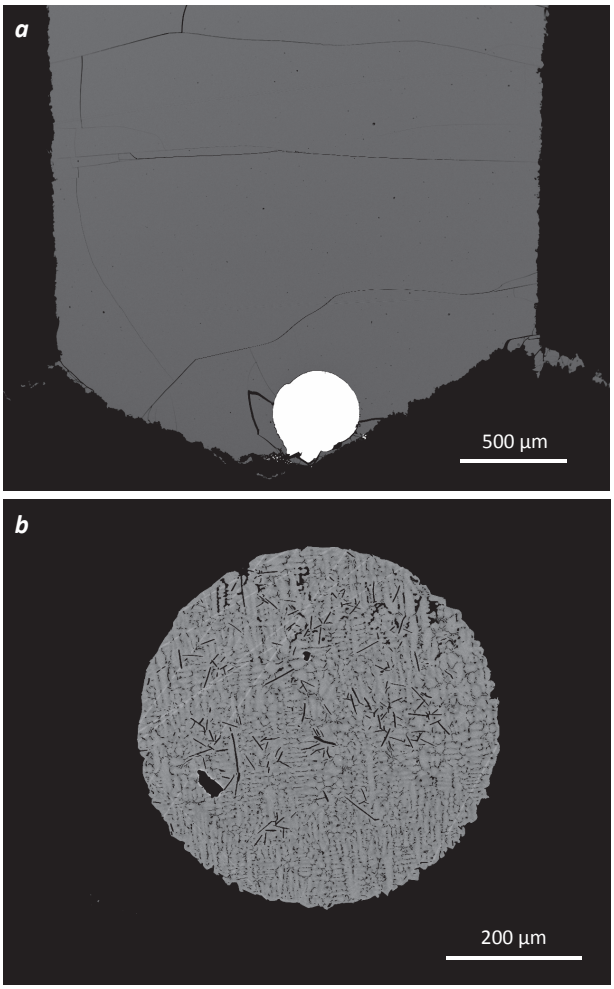
a
500 µm
b
200 µm

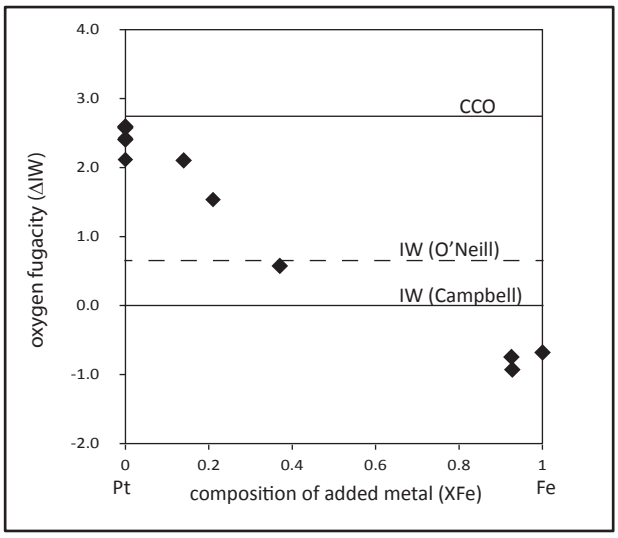
4.0
3.0
2.0
1.0
0.0
-1.0
-2.0
oxygen fugacity (ΔIW)
CCO
IW (O'Neill)
IW (Campbell)
0
0.2
0.4
0.6
0.8
1
Pt
composition of added metal (XFe)
Fe

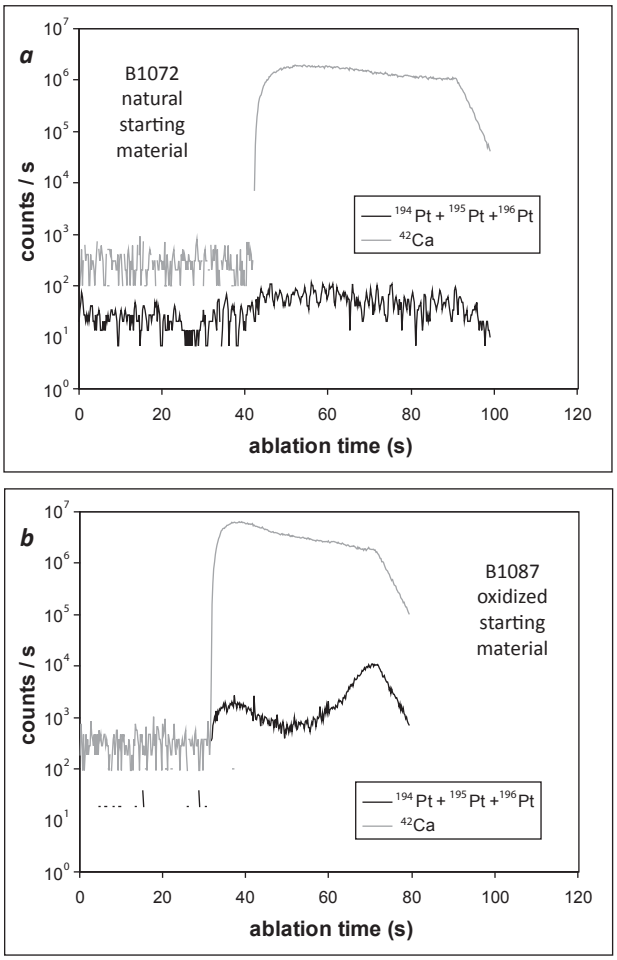
a
B1072
natural
starting
material
counts / s
ablation time (s)
194Pt + 195Pt + 196Pt
42Ca
b
B1087
oxidized
starting
material
counts / s
ablation time (s)
194Pt + 195Pt + 196Pt
42Ca

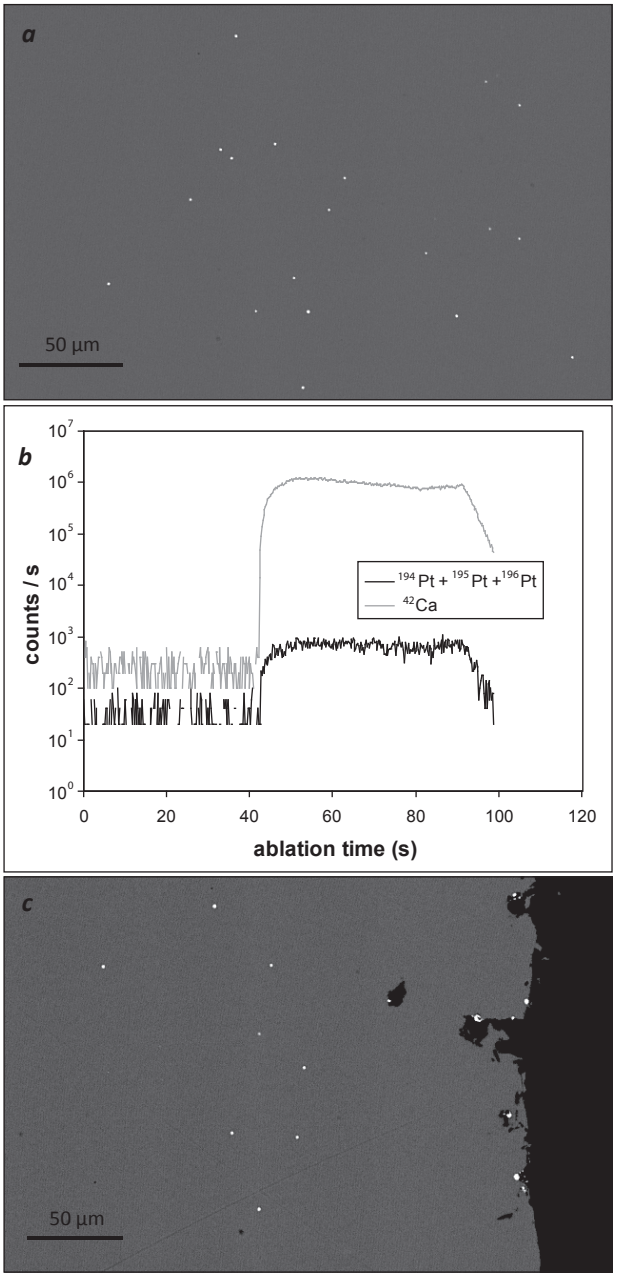
a
50 µm
b
counts / s
ablation time (s)
194Pt + 195Pt + 196Pt
42Ca
c
50 µm

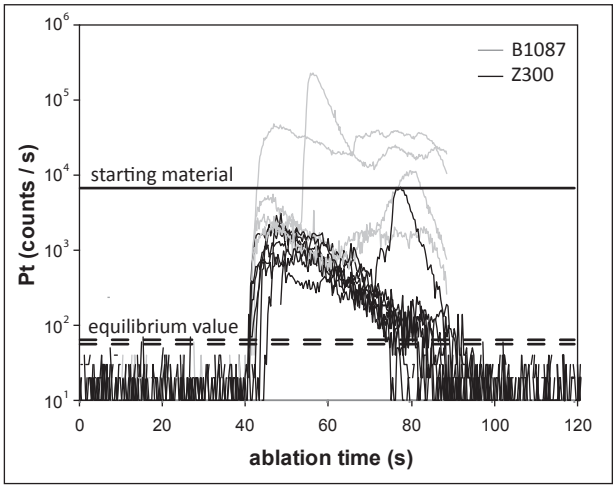
B1087
Z300
starting material
equilibrium value
Pt (counts / s)
ablation time (s)
10^6
10^5
10^4
10^3
10^2
10^1
0
20
40
60
80
100
120

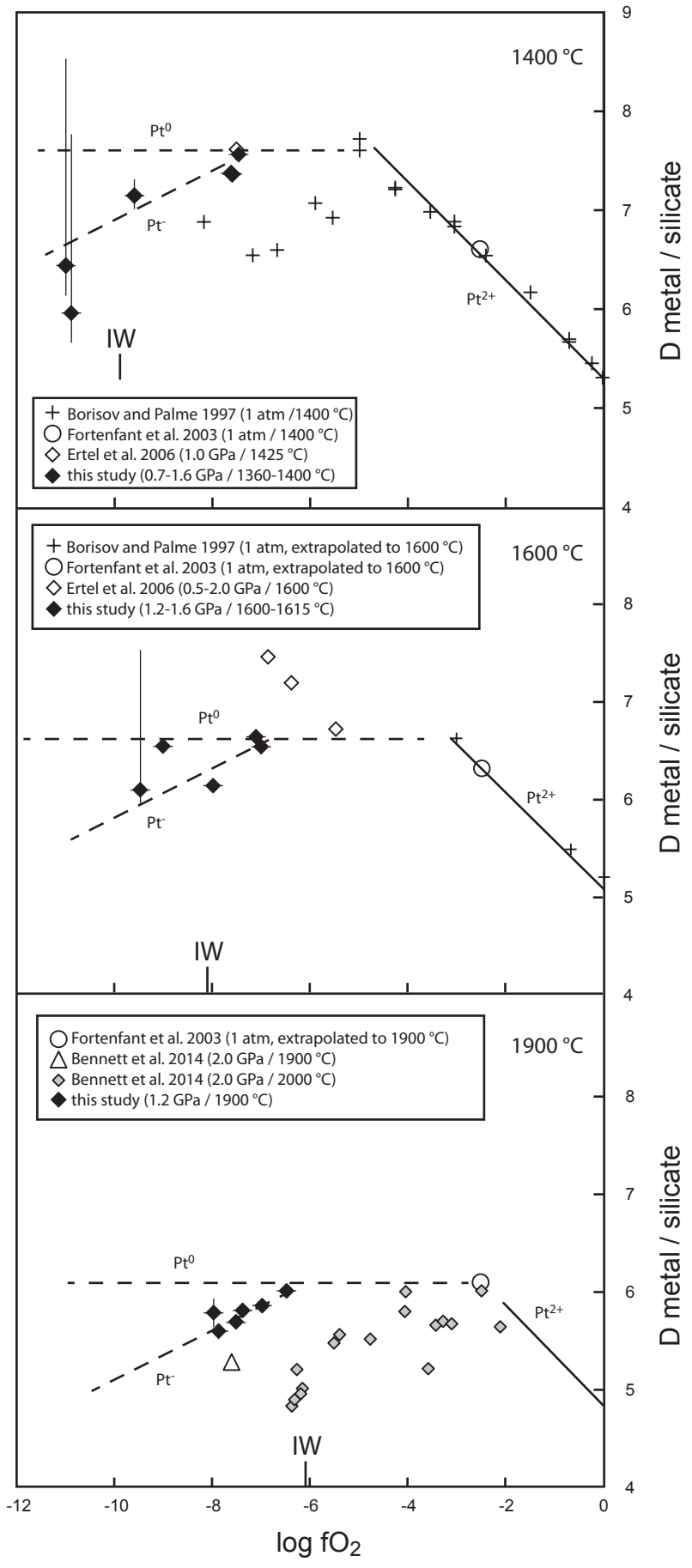
1400 °C
Pt0
Pt-
Pt2+
IW
Borisov and Palme 1997 (1 atm /1400 °C)
Fortenfant et al. 2003 (1 atm / 1400 °C)
Ertel et al. 2006 (1.0 GPa / 1425 °C)
this study (0.7-1.6 GPa / 1360-1400 °C)
1600 °C
Borisov and Palme 1997 (1 atm, extrapolated to 1600 °C)
Fortenfant et al. 2003 (1 atm, extrapolated to 1600 °C)
Ertel et al. 2006 (0.5-2.0 GPa / 1600 °C)
this study (1.2-1.6 GPa / 1600-1615 °C)
1900 °C
Fortenfant et al. 2003 (1 atm, extrapolated to 1900 °C)
Bennett et al. 2014 (2.0 GPa / 1900 °C)
Bennett et al. 2014 (2.0 GPa / 2000 °C)
this study (1.2 GPa / 1900 °C)
D metal / silicate
log fO2
-12
-10
-8
-6
-4
-2
0
4
5
6
7
8
9

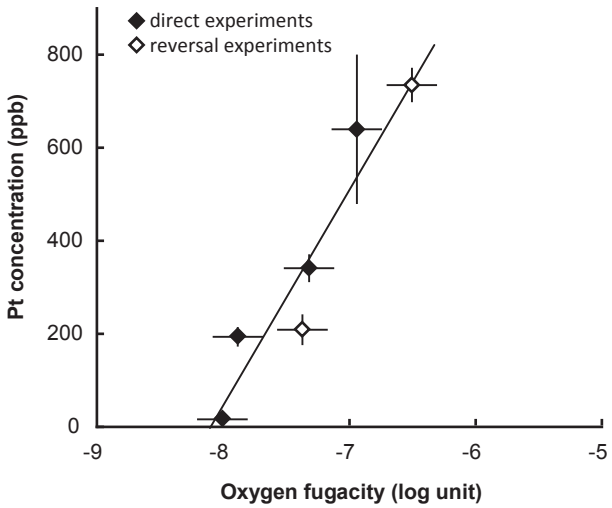
direct experiments
reversal experiments
800
600
400
200
0
-9
-8
-7
-6
-5
Pt concentration (ppb)
Oxygen fugacity (log unit)

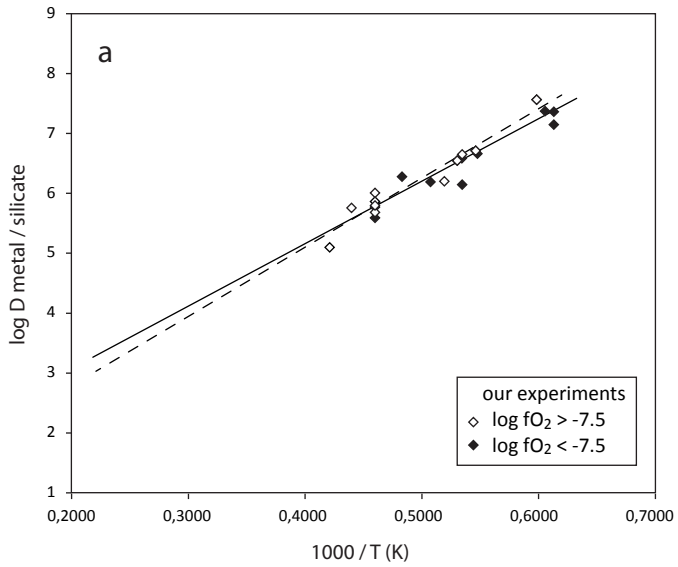
a
log D metal / silicate
1000 / T (K)
our experiments
log fO2 > -7.5
log fO2 < -7.5

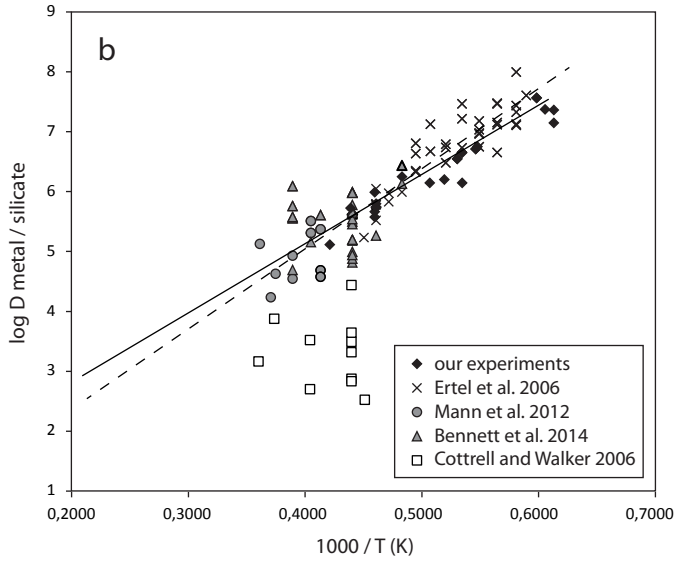
b
log D metal / silicate
1000 / T (K)
our experiments
Ertel et al. 2006
Mann et al. 2012
Bennett et al. 2014
Cottrell and Walker 2006

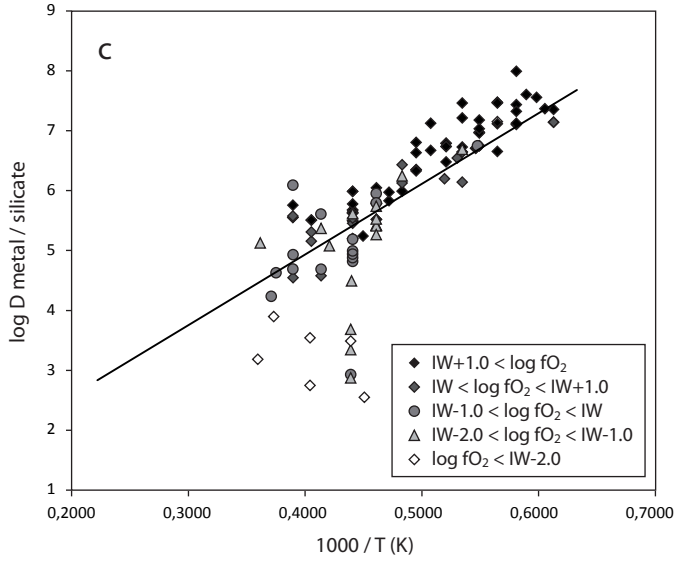
c
log D metal / silicate
1000 / T (K)
IW+1.0 < log fO2
IW < log fO2 < IW+1.0
IW-1.0 < log fO2 < IW
IW-2.0 < log fO2 < IW-1.0
log fO2 < IW-2.0